UNIVERSITÀ DEGLI STUDI DI PADOVA

Dipartimento di Fisica e Astronomia "Galileo Galilei"

Master Degree in Physics

Final Dissertation

Silicon based metalenses for generation and control of orbital momentum endowed light beams

Thesis supervisor

Prof. Filippo Romanato

Thesis co-supervisor

Dr. Andrea Vogliardi

Candidate

Alessandra Sabatti

Academic Year 2021/2022

Abstract

Metalenses are flat nanostructured devices capable of optically structuring light. Beam wavefronts can be shaped into helicoidal profiles, which provide light with orbital angular momentum (OAM). Here a spin multiplexing metalens is proposed. Unlikely common metasurfaces, this device transmits a different phase profile, an OAM wavefront and a constant phase respectively, according to the handedness of the input circular polarization of the beam. Its meta-unit structure is simulated with COMSOL software, and its design is realized by means of a customized MATLAB code. The metalens behaviour under gaussian beam illumination is then simulated, fulfilling the optical requirements. The device is fabricated through a master replica process adopting the nanoimprint lithography technique, after a nano-fabrication tuning procedure. The morphological features of the fabricated devices are analyzed via SEM imaging, showing a discrete adherence with the design. Eventually, the optical measurements confirm the presence of the double functionality: a gaussian and OAM beam can be independently generated according to the handness of the incoming light circular polarization, showing the possibility to control the light structure generated by bi-functional metalenses.

Contents

Chapter 1

Introduction

Regarding light beams, an interesting feature is the spatial distribution of their wavefront. In fact, the wavefront can be engineered to obtain a precise shape through the local modification of the phase of the electromagnetic wave. This process is known as light structuring and can be realized through the use of dedicated optics.
The most popular light structuring feature is the generation of helicoidal wavefronts, with the presence of the so called vortex singularity, which provides light with orbital angular momentum (OAM). This task can be achieved also in the visible wavelengths through the use of metalenses, flat nanostructured devices, which a few years ago introduces a revolution in optics. The metalenses turned out to be also very flexible in terms of multifunctionality.

A particular type of metalens can gives rise to a different wavefront structuring according to the incoming spin state of the beam. These devices are called dual-function metalenses due to the existence of two distinct spin states. This multiple functionality is possible due to the specific structure of the metalens, which is arranged in meta-units, each containing a nanofin with different shape and orientation. Unlike most common analogue devices, these metalenses are specifically designed to struture light through the modification of both its dynamical and geometrical phase.

The aim of this thesis work is the design, fabrication and characterization of this spin-multiplexing metalens, working at the wavelength of 775 nm. The device is realized on a glass substrate, since the lens works in the visible, with an amorphous silicon layer where the nanostructure pattern is reproduced.
The design process is carried out through a meta-units simulation with COMSOL fi-

nite element method analysis. The lens behaviour is then simulated with a customized MATLAB code. The fabrication is performed at CNR-IOM nanofabrication facility, through the technique of nanoimprinting lithography starting from an EBL master. The fabrication accuracy is evaluated via the analysis of SEM images of the metasurface. The device behaviour is then characterized by laser illumination and the quality of the intensity pattern is evaluated. The results show the capability of switching between two independent beams with different intensity profiles: a gaussian and an OAM beam, controlled by changing the handedness of the incoming circular polarization.
Lastly, the OAM generated by the metalens is compared with those produced by a commercial spiral phase plate device, and a q-plate previously nanofabricated with the same technique.

Among its applications, this metalens has a potential for contrast phase microscopy, since the illumination with a sample with an OAM endowed beam allows to enhance its structure by selectively enlightening its borders. The presence of a second gaussian beam function, would allow the rapid switching between contrast phase and classical illumination, realizing a flat, compact device able to carry out multiple functionalities, which provides new scenario in the possibility to design and fabricate optics with multi purpose applications.

Chapter 2

Beam optics theory

Light propagation can be described through the use of waves, mathematically represented by a real function of the position r = (x,y,z) and of time t, u(**r**,t). These functions are called **wavefunctions** and they are solution of the wave equation (which can be derived from Maxwell equations):

$$\nabla^2 u - \frac{1}{c^2}\frac{\partial^2 u}{\partial t^2} = 0 \tag{2.1}$$

where ∇^2 is the Laplacian operator, $\nabla^2 = \partial^2/\partial x^2 + \partial^2/\partial y^2 + \partial^2/\partial z^2$ and

$$c = \frac{1}{\sqrt{\epsilon_0 \mu_0}} = 3 \cdot 10^8 \frac{m}{s} \tag{2.2}$$

is the speed of light in vacuum. If Equation 2.1 is satisfied by a function $u(\mathbf{r})$, then u is an optical wave.
The simplest among these solutions is constituted by the monochromatic waves, whose time dependence is harmonic:

$$u(\mathbf{r}, t) = a(\mathbf{r}) cos[\omega t + \varphi(\mathbf{r})] \tag{2.3}$$

Where a(**r**) is the amplitude, $\phi(\mathbf{r})$ is the phase, $\omega = 2\pi f$ is the angular frequency [1].
A useful representation of the wavefunction is in the complex domain, using the **complex wavefunction**:

$$U(\mathbf{r}, t) = a(\mathbf{r}) e^{i(\omega t + \varphi(\mathbf{r}))} \tag{2.4}$$

Equation 2.3 is the real part of this function. Thus both these equations satisfy the wave equation with the same boundary conditions.

By factorizing the space- and time-dependent contributions of the complex wavefunction we obtain:

$$U(\mathbf{r},t) = U(\mathbf{r})e^{i\omega t} \tag{2.5}$$

U($\mathbf{r}$)=a($\mathbf{r}$)$e^{i\varphi(\mathbf{r})}$ is called **complex amplitude** of the wave and is the time-independent factor. Since the phase varies as a function of space, it is possible to define a set of points with equal phase value; these equal-phase surfaces are called **wavefronts**. The $\nabla\varphi(\mathbf{r})$, which is orthogonal to the wavefront, represents the direction of fastest phase variation. By substituting the complex wavefunction (2.5) into the wave equation (2.1), we find a condition for the complex amplitude, called **Helmoltz equation**:

$$(\nabla^2 + k^2)U(\mathbf{r}) = 0 \tag{2.6}$$

where $k = \frac{\omega}{c} = \frac{2\pi f}{c} = \frac{2\pi}{\lambda}$ is the wavenumber [1].
The intensity of a wave is given by the squared modulus of the complex amplitude:

$$I(\mathbf{r},t) = |U(\mathbf{r})|^2 \tag{2.7}$$

2.1 Paraxial waves

Speaking of wavefronts, if the waveront normal axes (parallel to $\nabla\varphi(\mathbf{r})$), are always approximately parallel to the propagation direction, the wave belongs to the family of **paraxial waves**. The most obvious example of a paraxial wave is the plane wave Ae^{-ikz}: by modulating its complex envelope A into a slowly varying function of position, A($\mathbf{r}$), it is possible to satisfy this condition. Thus the complex amplitude of a paraxial wave is:

$$U(\mathbf{r}) = A(\mathbf{r})e^{-ikz} \tag{2.8}$$

The restriction on the function A(r) assumes that the variation of A along a distance $\Delta z = \lambda$ is not comparable with the value of A. This translates into the following condition:

$$\frac{\Delta A}{\Delta z} << \frac{A}{\lambda} \rightarrow \frac{\partial A}{\partial z} << kA \tag{2.9}$$

Inserting the complex wavefunction amplitude 2.8 in the wave equation 2.1 we obtain the paraxial version of the Helmoltz equation:

$$\nabla_T^2 A - i2k\frac{\partial A}{\partial z} = 0 \tag{2.10}$$

where $\nabla_T^2 = \frac{\partial^2}{\partial x^2} + \frac{\partial^2}{\partial y^2}$ is the transverse laplacian operator, as its partial derivative are relative to the orthogonal components with respect to the propagation direction. We could neglect the term $k(\partial^2 A/\partial^2 z)$ in Equation 2.10 since it is smaller than other contributions. This can be seen from applying the derivative operation on both sides of Equation 2.9.
The constant solution $A = A_0$ to Equation 2.10 corresponds again to the plane wave.
Parabolical waves are a more general solution of equation 2.10:

$$A(\mathbf{r}) = \frac{A_0}{z} \exp\left(-ik\frac{r^2}{2z}\right) \tag{2.11}$$

where A_0 constant. The parabolical wavefronts of the beam are nothing but the paraxial approximation of spherical surfaces. [2].
The spherical waves, instead, are solutions of the first Helmoltz equation 2.6:

$$U(\mathbf{r}) = \frac{A_0}{r} \exp(ikr) \tag{2.12}$$

and do not respect the slowly varying condition 2.9.
Another solution, of crucial relevance in beam optics, is the **Gaussian beam**, whose complex envelope is:

$$A(\mathbf{r}) = \frac{A_0}{q(z)} \exp\left(-ik\frac{r^2}{2q(z)}\right) \tag{2.13}$$

where q(z) is the q-parameter:

$$q(z) = z + iz_R \tag{2.14}$$

being z_R the Rayleigh range. It's reciprocal can be defined as:

$$\frac{1}{q(z)} = \frac{1}{z + iz_R} = \frac{1}{R(z)} - i\frac{\lambda}{\pi w^2(z)} \tag{2.15}$$

where

$$R(z) = z\left[1 + \left(\frac{z - z_R}{z}\right)^2\right] \tag{2.16}$$

$$w(z) = w_0\sqrt{1 + \left(\frac{z}{z_R}\right)^2} \tag{2.17}$$

are respectively the wavefront curvature radius and the beam radius. Then the complex

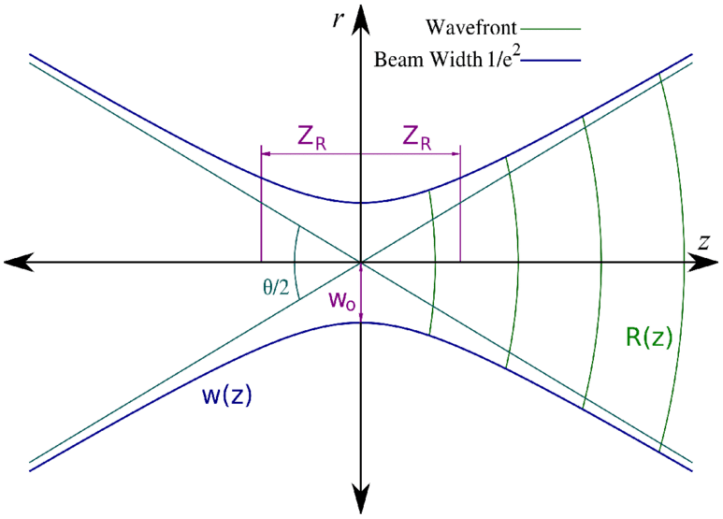

Figure 2.1: Representation of gaussian beam in correspondence of its beam waist. The beam radius and the Rayleigh range are represented, as well as the divergence angle. [3]

amplitude acquires the following form:

$$E(r,\varphi,z) = E_0 \frac{w_0}{w(z)} exp\left(-\frac{r^2}{w^2(z)}\right) exp\left(-ikz - ik\frac{r^2}{2R(z)} - i\zeta(z)\right) \tag{2.18}$$

where

$$\zeta(z) = tan^{-1}\left(\frac{z}{z_0}\right) \tag{2.19}$$

is the so called Gouy phase.

$w_0 = w(z=0)$ is the beam waist, as it indicates the minimum diameter of the beam. At the beam radius calculated in correspondence of Rayleigh range: $w(z_R)$, the beam radius assumes the value of $w(z_R) = \sqrt{2}w_0$. The relationship among these quantities is:

$$w_0 = \sqrt{\frac{\lambda z_R}{\pi}} \tag{2.20}$$

From this equation we can see the proportionality between the waist and z_R.
From the equation for the beam radius R(z) we can see that, when z tends to zero, the wavefront curvature radius tends to infinity, which means that the wavefront is planar, like for plane waves. For z going to infinity, R(z) tends to z, like in spherical surfaces. So the gaussian beam can be approximated with a plane wave at the waist and with a spherical surface far from its waste. The minimum curvature radius is in correspondence

of $z = z_R$:

$$R(z) = \begin{cases} \to +\infty & z \to 0 \\ 2z_R & z = z_R \\ \sim z & z \to +\infty \end{cases} \tag{2.21}$$

The gaussian beam intensity is:

$$I(r,z) = |A_0|^2 \left[\frac{w_0}{w(z)}\right]^2 \exp\left[-\frac{2r^2}{w^2(z)}\right] \tag{2.22}$$

At any value of z, the intensity is a Gaussian function, hence the definition of Gaussian beams. [2]

2.2 Laguerre-Gauss beams and Optical Angular Momentum

There are different complete sets of solutions for Equation 2.10, which means that any other solution can be expressed as a linear superposition of their components. A great number of solutions are known for the paraxial wave equation and many of these are routinely used to describe laser fields, including Gaussian beams and the higher-order Hermite–Gaussian modes. Of especial interest to us, however, are the Laguerre–Gaussian solutions. It is more convenient to express them in cylindrical polar coordinates (r, φ, z) and they take the form [4]:

$$\begin{aligned} U_{l,p}(r,\varphi,z) = A_{l,p}\left[\frac{w_o}{w}\right]\left(\frac{r}{w(z)}\right)^{|l|} L_p^{|l|}\left(\frac{2r^2}{w^2(z)}\right) exp\left[-\frac{r^2}{w^2(z)}\right] \times \\ \times exp\left[-ikz - ik\frac{r^2}{2R(z)} + il\varphi + i(l+2p+1)\zeta(z)\right] \end{aligned} \tag{2.23}$$

where $L_p^{|l|}$ is an associated Laguerre polynomial. The $e^{il\varphi}$ phase term found in the Laguerre-Gauss beam expression generates a continuous helicoidal wavefront structure, with l equispaced intertwined lobes that rotate around the optical axis.
Each solution is identified by the couple of indices (p, l): p is the radial index, identifies the number of radial nodes, l represents the number of intertwined helical phasefronts. The intensity is circularly symmetric, with a central dark singularity. The wavefronts assume a helical form with helicity given by the sign of l. l is also called topological charge of the beam.

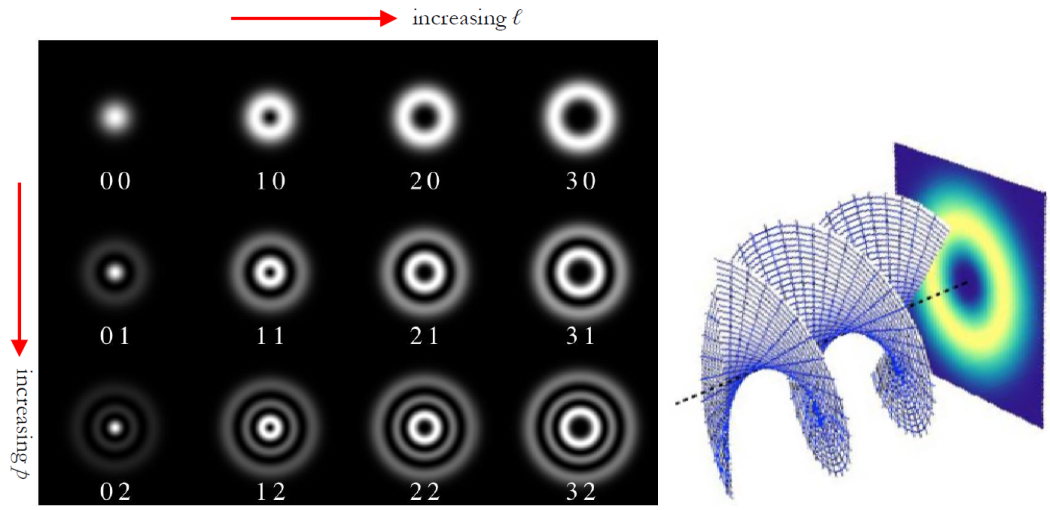

Figure 2.2: Intensity transverse profiles of Laguerre-Gaussian beams, as a function of the indices l,p (left) [5]. Representation of helicoidal wavefront due to the term $e^{il\varphi}$.

If we traverse a closed path around the propagation axis then we a accumulate a phase of 2π [6]. This azimuthal phase dependence is familiar from quantum theory, since this wave function is an eigenstate of the orbital angular momentum (OAM) operator

$$\hat{L}_z = -i\hbar\frac{\partial}{\partial\phi}, \tag{2.24}$$

with eigenvalue $l\hbar$. In fact each photon in a Laguerre–Gaussian laser beam of the form 2.23 carries an orbital angular momentum of $l\hbar$ [4][7].

Light beams carrying OAM always embed an optical vortex (OV) along the beam axis. From a mathematical point of view, OVs are wavefront dislocations, with peculiar topological properties, that arise due to phase singularities in the optical field. Light beams with an embedded OV are universally characterized by a dark central region, a consequence of destructive interference phenomena that gives the beam the typical doughnut-shaped intensity distribution [8].
OVs have many applications of great interest: some are reported in the following. Their angular momentum makes possible to transmit a rotational moment to physical micro-scaled objects. They can be applied to contrast phase microscopy, since they allow to transmitting only high frequency in a Fourier-filtering setup. They can be applied to STED microscopy: the annular region with very high intensity excites the flourophores at the borders of the detection region, so that an observation window in the central region is created, and super-resolution microscopy can be obtained [9]. They also have

application for fibre optic signal multiplexing in telecommunications. Due to these variety of applications, many techniques for generating them have been proposed.
Spin Angular Momentum (SAM) of light and OAM are not the same. The orbital and spin parts of the angular momentum are, respectively,

$$\begin{aligned} \mathbf{L} &= \int \sum_j E_j(\mathbf{r} \times \nabla) A_j \mathrm{dV} \\ \mathbf{S} &= \int \mathbf{E} \times \mathbf{A} \mathrm{dV} \end{aligned} \tag{2.25}$$

where $\mathbf{E}$ is the electric field and $\mathbf{A}$ is the transverse (i.e. divergenceless) part of the vector potential. [4]
Te SAM is related to the vectorial nature of the EM field. There are two possibel states: $\pm\hbar$ if referring to single photon, left and right circular polarization if referring to classical light. The OAM, instead, is related to the spatial distribution of the phase structure: Infinite discrete states exist with value $\pm n\hbar$ if referring to single photon, helical wavefront with n intertwined fronts, with positive or negative helicity.

2.3 Light polarization

Speaking of polarization of an electromagnetic wave, we refer to the direction of its electrical component and its evolution with wave propagation.
If the direction of the field remains fixed as the wave moves forward, the light is **linearly polarized**. The plane of polarization is defined as the plane containing $\vec{E}$ and the direction of propagation. The plane polarized light represented can be described by the equation:

$$\vec{E}(z,t) = \vec{E_0} e^{i(kz-\omega t)} \tag{2.26}$$

where $\vec{E}$ can have any direction in the plane orthogonal to the propagation direction.
Similarly, we can sum two plane waves with orthogonal linear polarizations, but differing of a phase δ:

$$\vec{E}(z,t) = \hat{i} E_{0x} e^{i(kz-\omega t)} + \hat{j} E_{0y} e^{i(kz-\omega t+\delta)} \tag{2.27}$$

If $\delta = \pm\frac{\pi}{2}$ the light is respectively left or right circularly polarized, as the direction of $\vec{E}$ rotates in the transverse plane.
If the moduli of the fields of the orthogonal components are different: $E_{0x} \neq E_{0y}$, or the phase retardation is different from $\pm\frac{\pi}{2}$, or both, the resulting electric field describes an ellipse: we speak about elliptical polarization.

2.4 Polarizers and wave plates

A polarizer is an optical element that can accept as input non polarized light, or natural light, and whose output is polarized light. Among the others, they can exploit the directional absorption of polymer chains (dichroism) or be based on birefringence or reflective polarization. [10]
A **linear polarizer** is a device that can turn non-polarized light into a light that is linearly polarized, i.e. its electric field oscillates along a constant direction axis, the transmission axis. The transmitted intensity as a function of the angle θ between the transmission axes of two consecutive linear polarizers is described by the Malus law:

$$I_t(\theta) = I_0 \cos^2(\theta) \tag{2.28}$$

the second polarizer can be called analyzer, since by sampling all possible rotations, it is possible to obtain information about the first polarization (Figure 2.3).

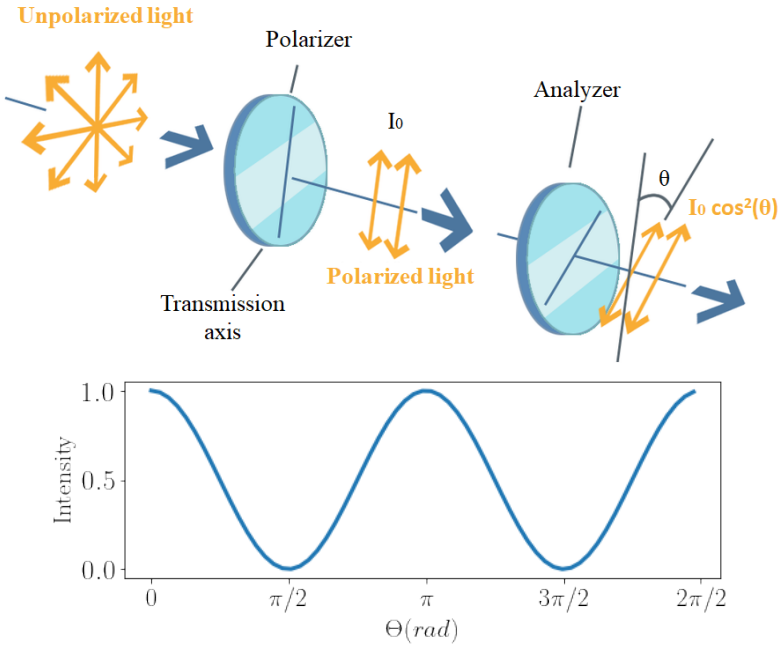

Figure 2.3: Representation of phenomenon described by Malus law [11] and plot of transmitted intensity as a function of the angle between polarizer and analyzer.

When light passes through a medium its velocity v changes with respect to its velocity in the vacuum c. Their ratio is the refractive index $n = c/v$. In general, in a crystal, it is possible to have, for each direction of $\hat{k}$ vector, two possible values for the refractive index,

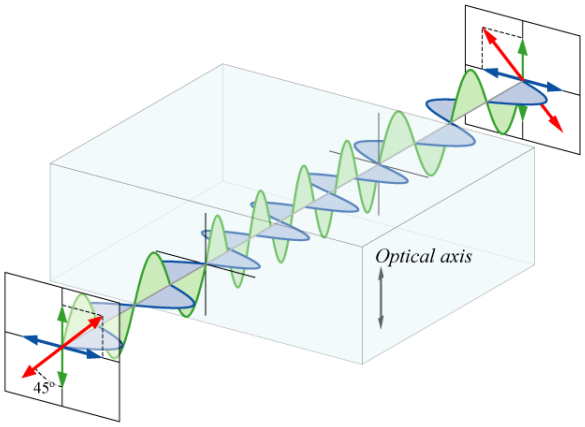

Figure 2.4: Scheme of half wave plate functioning. [12]

corresponding to orthogonal polarization states. Birefringence is due to anisotropies within a crystal, or a crystal-like structure, since the unit-cell can be non-symmetric. This means that light propagates with different velocities in the material according to the direction taken.

If we consider a birefringent material oriented in such a way that its refractive index is n_x along the x-axis and n_y along the y-axis, a wave propagating in this medium will see a phase difference in its components due to the optical path difference:

$$\Delta\Phi = k\Delta L = \frac{2\pi}{\lambda} d(n_y - n_x) \tag{2.29}$$

If the phase difference (Equation 2.29) is equal to $\pi/2$, then the optical path is equal to a quarter of the wavelength:

$$d(n_y - n_x) = \frac{\lambda}{4} \tag{2.30}$$

Hence this device allows to realize circular polarization. If the phase difference of Equation 2.29 is equal to π instead, the optical path is equal to a half of the wavelength, and we speak about half wave plate:

$$d(n_y - n_x) = \frac{\lambda}{2} \tag{2.31}$$

This device turns an input linear polarization with angle α with respect to the fast axis, into a linear polarization of angle 2α. This means that the y-component is flipped with respect to the optical axis (Figure 2.4). Polarizers and wave plates will be useful for the functioning and characterization of metalenses.

Jones matrix formalism

Given the electric field of a generic elliptically polarized plane wave:

$$\vec{E_0} = \hat{i}E_{0x} + \hat{j}E_{0y} \tag{2.32}$$

with E_{0x}, $E_{0y} \in \mathbb{C}$, and being $\hat{i}$, $\hat{j}$ the versors oriented along x and y axes, the Jones' notation for this vector is:

$$\vec{E_0} = \begin{bmatrix} E_{0x} \\ E_{0y} \end{bmatrix}$$
$$\vec{E_0'} = \frac{1}{\sqrt{|E_{0x}|^2 + |E_{0y}|^2}} \begin{bmatrix} E_{0x} \\ E_{0y} \end{bmatrix}$$

where $\vec{E_0'}$ is the normalized version of the Jones vector. Any optical element acting on the polarization state can be described as a 2x2 matrix:

$$\begin{bmatrix} A' \\ B' \end{bmatrix} = \begin{bmatrix} a & b \\ c & d \end{bmatrix} \begin{bmatrix} A \\ B \end{bmatrix} \tag{2.33}$$

where the *abcd* matrix can also be the product of the matrices of an ensemble of optical elements, starting from the last one acting on the beam.

In the following a list of the optical elements, in Jones representation, that will be useful for the optical characterization for the metalenses object of this thesis is reported.
Linear polarizer:

$$\begin{bmatrix} 1 & 0 \\ 0 & 0 \end{bmatrix} \text{ Horizontal transmission axis} \tag{2.34}$$
$$\begin{bmatrix} 0 & 0 \\ 0 & 1 \end{bmatrix} \text{ Vertical transmission axis}$$

Generic phase retarder:

$$\begin{bmatrix} 1 & 0 \\ 0 & e^{i\delta} \end{bmatrix} \tag{2.35}$$

Quarter wave plate:

$$\frac{1}{\sqrt{2}}\begin{bmatrix} 1 & \mp i \\ \mp i & 1 \end{bmatrix} \quad \text{Fast axis at } \pm 45° \tag{2.36}$$

A circular polarization is obtained when a linearly polarized beams' components, of equal intensity, undergo a phaseshift of $\pi/2$.

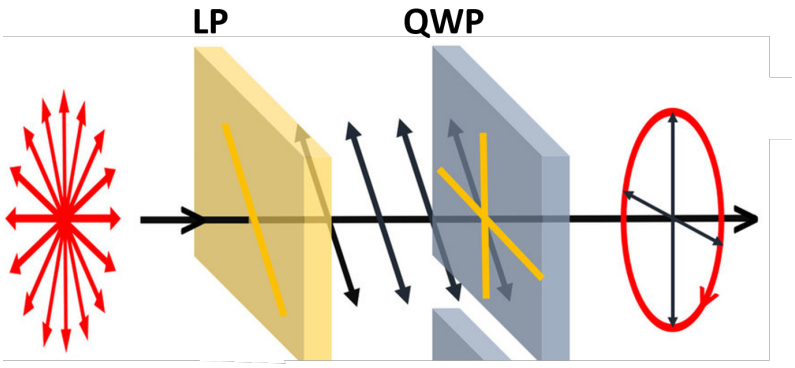

Figure 2.5: Scheme for the realization of a circular polarization. [13]

With Jones' matrix formalism, this can be seen as a QWP, with fast axis at $\pm 45°$, acting on a vertical linearly polarized wave, as shown by the scheme in Figure 2.5:

$$\frac{1}{\sqrt{2}}\begin{bmatrix} 1 & \mp i \\ \mp i & 1 \end{bmatrix}\begin{bmatrix} 0 \\ 1 \end{bmatrix} = \frac{\mp i}{\sqrt{2}}\begin{bmatrix} 1 \\ \pm i \end{bmatrix} \rightarrow \frac{1}{\sqrt{2}}\begin{bmatrix} 1 \\ \pm i \end{bmatrix} \tag{2.37}$$

The result is a wave respectively LCP or RCP.

Chapter 3

Metalenses

3.1 From diffractive optics to metalenses

Diffractive optical elements (DOE) exploit the wave periodicity to reproduce the phase transmitted by classic bulk refractive optical elements in flat devices whose maximum thickness is

$$d_{\max} = \frac{\lambda}{n-1} \tag{3.1}$$

where n is the material refractive index.

An example of DOE is the spiral phase plate (SPP). The SPP is a helicoidal transmission element imposing an azimuthally dependent phase delay on an incident optical wavefront, while preserving the direction of the optical axis. It is a transparent plate, looking like a spiral staircase, in which the thickness increases around the central axis of the plate. [8] [14].
In Figure 3.1 it is possible to see that this staircase has a discontinuity along one radius of the element. The total phase gap straddling the discontinuity can be written as:

$$2\pi l = \frac{2\pi}{\lambda}(n_{\mathrm{SPP}} - 1)h_{tot} \tag{3.2}$$

which means that the staircase height h must be:

$$h(\lambda) = \frac{\lambda}{(n_{\mathrm{SPP}} - 1)}l \tag{3.3}$$

SPPs are thus built for a specific wavelength λ at which the minimum intensity in cor-

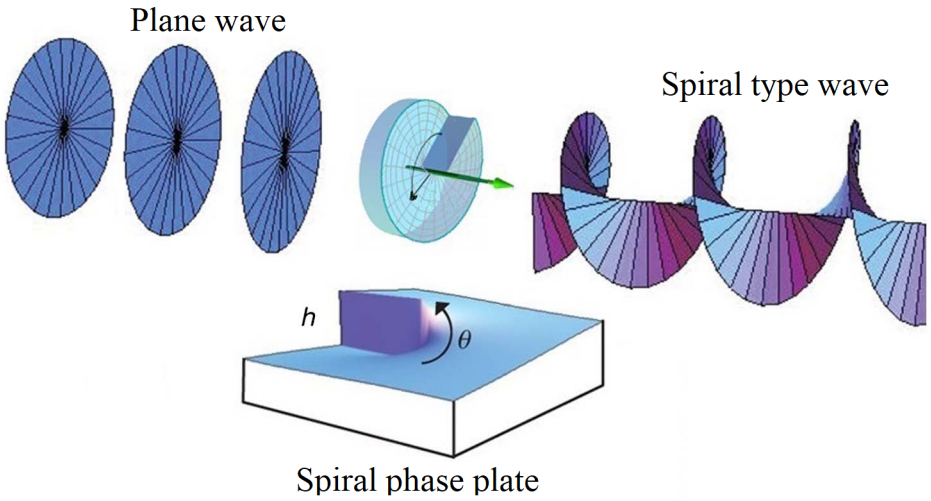

Figure 3.1: Scheme and functioning of a SPP. [15]

respondence of the optical axis is obtained. Therefore, the height of the spiral needs to be precisely engineered to produce the desired topological charge from the incident wavelength. [8]
The output carrying-OAM beam can be described as a Laguerre-Gaussian beam (Described in section 2.2) [15].
Their disadvantage consists the difficulty in patterning three-dimensional structures in materials like silicon, which is the disadvantage of DOEs in general.
To overcome these limitations, metasurfaces (or metalenses) have been proposed with different categories according to their design, which can be based on patterns composed by gratings or by meta-units, and involve the exploitation of dynamic phase, geometric phase, or both.

A **metalens** is an advanced flat optical device composed of artificial antennas. The amplitude, phase, and polarization of incident light can be engineered in order to obtain an output wave with the desired features. Metalenses can be designed to achieve a variety of functions, such as diffraction-limited focusing, high focusing efficiency, and aberration correction, which are useful in various application scenarios. [16]
A key goal of metalens research is to achieve light wavefront shaping using optical elements with thicknesses of the order of the wavelength. Such miniaturization is expected to lead to compact, nanoscale optical devices with applications in cameras, lighting, displays and wearable optics. [17]

3.1.1 Dynamic phase manipulation

Metasurfaces based on dynamic phase manipulation are composed by meta-units of fixed dimensions, with embedded structures called nanofins (those are a sort of pillars, see Figure 3.2) which change point-wise their dimensions. This change results into a local variation of the effective refractive index. The in plane dimensions of the pillar change isotropically, while the off-plane one is comparable to the wavelength and is fixed for the entire pattern. The design parameter is represented by the filling factor f(x,y) also called duty cycle, i. e. the ratio between the width of the feature and the period. The transmission function of a meta-unit as a function of its in-plane position is:

$$t(x, y) = e^{i\Omega(x,y)} \tag{3.4}$$

$$\Omega(x, y) = k_0 d(n_{\text{eff}}(x, y) - 1) \tag{3.5}$$

where $\Omega(x; y)$ is the desired phase pattern as a function of the planar position on the metasurface [18]. As deductible from Equation 3.4, the phase pattern can be obtained through the engineering of the effective refractive index, which is controlled by the local filling factor f(x,y). There are several theories for relating the filling factor to a medium made of two materials (the first material is the one composing pillars, the second one is air), those are called effective medium theories [19].

3.1.2 Geometric phase manipulation

Metaunits can also be anisotropic in the in-plane dimensions, i.e result in different effective refractive indices for different orthogonal TE and TM polarizations n_{TE}, n_{TM}. The differentce between the designs is illustrated in Figure 3.2. With an anisotropic unit, light locally undergoes to a phase retardation expressed by $\tau(x, y)$:

$$\tau = \begin{bmatrix} e^{ikdn_x} & 0 \\ 0 & e^{ikdn_y} \end{bmatrix} = e^{-ikd(n_x+n_y)/2} \begin{bmatrix} e^{-i\delta/2} & 0 \\ 0 & e^{+i\delta/2} \end{bmatrix} \tag{3.6}$$

where $\delta = \frac{2\pi}{\lambda} d(n_y - n_x)$ [22].

An other key degree of freedom is the element rotation. The phase retardation matrix of equation 3.6 is then rotated according to the orientation of the nanofin inside the meta-unit. In the design of this kind of metalens, the orientation of the meta-unit nanofin

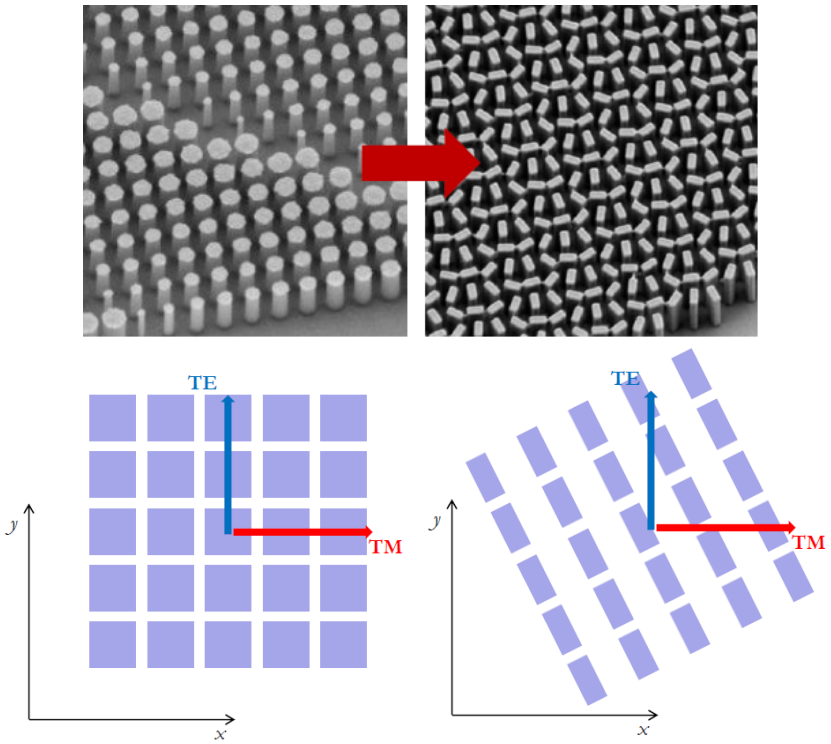

Figure 3.2: Left: difference between dynamic phase metalens (composed of cylindrical pillars of different radius) and geometrical phase (PB) metalens.[20] [21] Right: Comparison between effective refractive index for isotropic and constant oriented meta-units, and anisotropic and rotated meta-units.

itself varies with its position in the plane (x,y). So the transmission matrix becomes:

$$T(x,y) = R\tau(x,y)\tau(\delta)R^{-1}(x,y) \tag{3.7}$$
$$R = \begin{bmatrix} \cos\theta(x,y) & \sin\theta(x,y) \\ \sin\theta(x,y) & \cos\theta(x,y) \end{bmatrix}$$

The principle of these optics consists in changing point by point on the surface the extraordinary axis orientation of the effective uniaxial structure [22].

Identical meta-units

If the structure is composed by identical meta-units with different orientations, the phase retardation δ between the element orthogonal axes remains constant. It is interesting to apply the transmission matrix of Equation 3.7 to circularly polarized light:

$$T\begin{pmatrix} 1 \\ \pm i \end{pmatrix} = \cos\left(\frac{\delta}{2}\right)\begin{pmatrix} 1 \\ \pm i \end{pmatrix} - i\,\sin\left(\frac{\delta}{2}\right)e^{\pm 2i\theta}\begin{pmatrix} 1 \\ \mp i \end{pmatrix} \tag{3.8}$$

In this representation, the resulting wave consists of two components: the zero-order, exhibiting the same polarization of the incident beam and no phase modification, and the diffracted order, exhibiting an orthogonal polarization and a phase term equal to twice the local orientation of the unit, with a sign depending on the input handedness. The second contribution is an orthogonally-polarized term carrying a phase modulation equal to twice the orientation angle of the optic axis, with sign depending on the input polarization. [22] This phase modulation is called **Pancharatman Berry phase**, and the elements manipulating light with this feature are called Pancharatman-Berry opical elements (PBOE). Their fundamental feature is the spatially variant artificial birefringence.
The first zero-order term is proportional to $cos(\delta/2)$, thus its value is zero when $\delta = \pi$:

$$T\begin{bmatrix} 1 \\ \pm i \end{bmatrix} = -ie^{\pm 2i\theta}\begin{bmatrix} 1 \\ \mp i \end{bmatrix} \tag{3.9}$$

Therefore, if the meta-units behave like half wave plates, the incident polarization is completely conversed into its orthogonal one. If the aim is to transfer the phase-pattern $\Omega(x,y)$ with maximum efficiency, the metasurface should implement half-wave plate elements inside each meta-unit with an orientation of their extraordinary axis of $\theta(x,y) = \Omega(x,y)/2$. Thus, the half wave plate condition translates into the maximum efficiency for the phase pattern Ω realization.

Meta-units with variable dimensions

Considering pillars of different dimensions and orientations, it is possible to act simultaneously on the dynamic and geometric phase.
For circularly polarized incident waves, P-B phase has been widely explored for metasurface design to flexibly manipulate electromagnetic wavefronts. Nevertheless, the intrinsic nature of the P-B phase produces antisymmetrical (equal and opposite) response characteristics between orthogonal circularly polarized states, which means that the right-handed and left-handed circularly polarized waves cannot be independently manipulated by applying the spatial phase function achieved with only the geometric phase. [23]. Recently, it has been demonstrated that the orthogonal polarization states of the wavefronts can be modulated independently by synthesizing the propagation phase and geometrical phase. This is the basic principle of dual function metalenses.[23]

3.2 Dual function metalenses

Regarding miniaturized and integrated systems, a single flat device that possesses diversified functionalities is highly desirable in optical to microwave regimes. With this perspective, bifunctional metalenses constructed by meta-atoms with integrated response to propagation phase and geometric phase are proposed for independent manipulation of right-handed and left-handed circularly polarized waves. [23].

Suppose that, for left and right circular polarizations $|L\rangle = [1\ i]^T$ and $|R\rangle = [1\ -i]^T$, the desired phase patterns are respectively $\phi^+(x,y)$ and $\phi^-(x,y)$.
If $\phi^+(x,y) = -|\phi^-(x,y)|$ there is complete asymmetry between orthogonal polarization state and we recover classical PB based lenses.
In the more general case, it can be demonstrated [23] that the transmission function (or Jones matrix) for a meta-atom in position (x,y), given the two phase patterns, is:

$$J(x,y) = \frac{1}{2}\begin{bmatrix} e^{i\phi^+(x,y)} + e^{i\phi^-(x,y)} & -i\cdot e^{i\phi^+(x,y)} + i\cdot e^{i\phi^-(x,y)} \\ -i\cdot e^{i\phi^+(x,y)} + i\cdot e^{i\phi^-(x,y)} & -e^{i\phi^+(x,y)} - e^{i\phi^-(x,y)} \end{bmatrix} \tag{3.10}$$

This matrix can represent the Jones function of the whole metalens, considering its action point-wise on the surface coordinates (x,y). This can be demonstrated in the following way. The transmission function acts on the two circular polarization states as:

$$\begin{aligned} J(x,y)|L\rangle &= e^{i\phi^+}|R\rangle \\ J(x,y)|R\rangle &= e^{i\phi^-}|L\rangle \end{aligned} \tag{3.11}$$

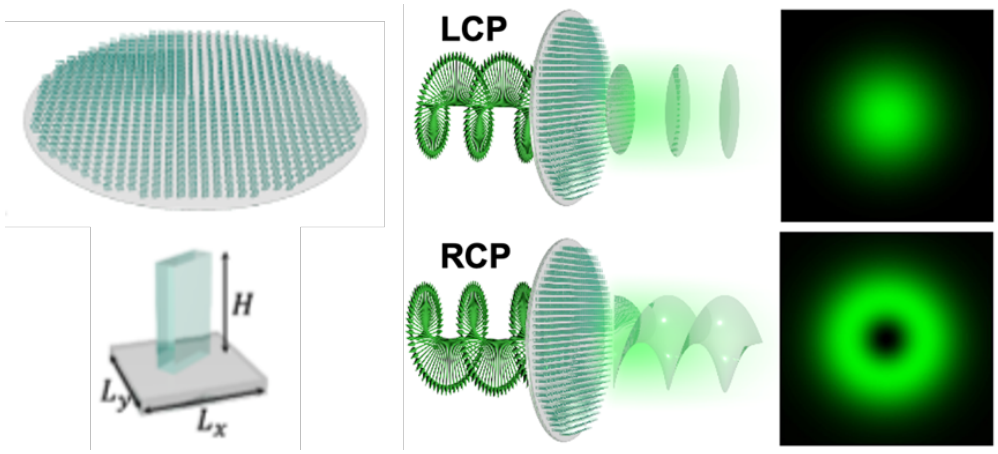

Figure 3.3: Graphical representation of meta-atoms lens and single pillar (left). Illustration of dual-functioning of the ML under opposite circular polarization; the two exemplified functions are a gaussian beam and an OAM beam (right). [24]

So the matrix J acting on the matrix whose columns contain the Jones vectors for the left and right polarizations must respect:

$$J(x,y)\begin{bmatrix}1 & 1\\ i & -i\end{bmatrix} = \begin{bmatrix}e^{i\phi^+} & e^{i\phi^-}\\ -i\cdot e^{i\phi^+} & i\cdot e^{i\phi^-}\end{bmatrix} \tag{3.12}$$

which can be rewritten as:

$$\begin{aligned} J(x,y) &= \begin{bmatrix}e^{i\phi^+} & e^{i\phi^-}\\ -i\cdot e^{i\phi^+} & i\cdot e^{i\phi^-}\end{bmatrix}\begin{bmatrix}1 & 1\\ i & -i\end{bmatrix}^{-1} = \\ &= \frac{1}{2}\begin{bmatrix}e^{i\phi^+(x,y)} + e^{i\phi^-(x,y)} & -i\cdot e^{i\phi^+(x,y)} + i\cdot e^{i\phi^-(x,y)}\\ -i\cdot e^{i\phi^+(x,y)} + i\cdot e^{i\phi^-(x,y)} & -e^{i\phi^+(x,y)} - e^{i\phi^-(x,y)}\end{bmatrix} \end{aligned} \tag{3.13}$$

By carrying out the matrix multiplication in the right-hand side of Equation 3.13 we find the expression for J(x,y) matrix, as reported in Equation 3.10. [16],[24]

Our task is now to relate the transmission matrix to the meta-unit bi-refringence and the local orientation of the pillars. In particular we want to relate the phases ϕ^+ and ϕ^- to the retardations δ_x and δ_y of the bi-refringent pillars, and to the pillar orientation angle θ.

The matrix J is unitary, thus it can be diagonalized by a matrix A such that $J = Q^{-1}AQ$:

$$A = \begin{bmatrix} e^{[\frac{1}{2}(\phi^+(x,y)+\phi^-(x,y))]} & 0 \\ 0 & e^{[\frac{1}{2}(\phi^+(x,y)+\phi^-(x,y))-\pi]} \end{bmatrix}$$
$$Q = \begin{bmatrix} \cos\theta(x,y) & \sin\theta(x,y) \\ -\sin\theta(x,y) & \cos\theta(x,y) \end{bmatrix} = R\left[\theta(x,y)\right]$$
$$\theta(x,y) = R\left[\frac{1}{4}(\phi^+(x,y) - \phi^-(x,y))\right]$$

where A is the matrix containing the eigenvectors of J, and the columns of Q are J's eigenvectors.
Therefore J is a matrix composed by a rotated phase retarder, exactly like the transmission matrix of the PBOE in Equation 3.7. The physical interpretation is analogue, so the diagonal entries of A correspond to the phase delays along x- and y- direction provided by the meta-atom, while the angle of the rotation matrix indicated the orientation of the meta-atom.

$$\delta_x = \frac{1}{2}(\phi^+(x,y) + \phi^-(x,y))$$
$$\delta_y = \frac{1}{2}(\phi^+(x,y) + \phi^-(x,y)) - \pi$$

and the orientation angle must respect:

$$\theta = \frac{1}{4}(\phi^+(x,y) - \phi^-(x,y)) \tag{3.14}$$

This way the transmitted phases δ_x and δ_y represent the bi-refringence of the pillars as a function of the desired pattern phases ϕ^+ and ϕ^-. They differ of π in order to achieve the maximum conversion efficiency in transmission with circularly polarized waves, like for PBOE [16], [24] [25].

In practice this birefringence is a function of the spatial coordinate (x,y). This feature is achieved by varying x and y dimensions of the pillars, and their overall shape (Figure 3.4). Therefore we need a library of meta-atoms with different geometries in term of shapes and dimensions of the pillars.
In order to be able to realize any desired phase profile, we need δ_x and δ_y to cover the entire range $[0; 2\pi]$.

The simulation and optimization of the single metaunit is usually performed numerically, choosing among different methods. The methods used for this work will be illustrated

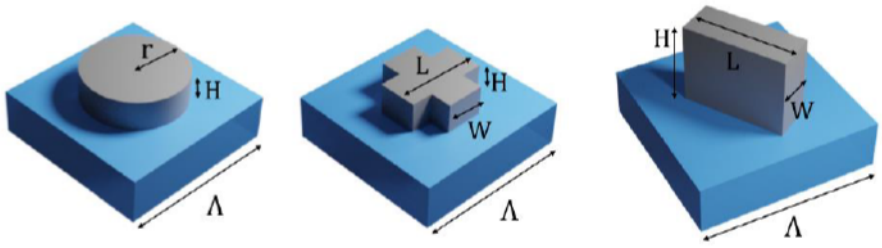

Figure 3.4: Example of different pillar shapes for the meta-units. Λ is the periodicity parameter. [18]

in Chapter 4. For a given material and geometry, the optimization of the metaunit parameters is performed in terms of conversion efficiency (π-delay condition) and transmittance/reflectance proportion. The pillars can also present different geometries in order to increase the degrees of freedom for fulfilling these requests, as shown in Figure 3.4.

3.3 Birefringent sub-wavelength gratings

The form-birefringence can be induced by introducing space-variant subwavelength gratings in combination with the local control of their orientation. [22] Such gratings can be arranged in pixels, similarly to diffractive and refractive elements. They also can be designed as continuously-variant gratings, without this subdivision.
Also gratings have different refractive index in the direction parallel (n_{TE}) and perpendicular (n_{TM}) to the grating direction. They behave exactly like PBOE. The phase difference introduced by a PBOE between the two polarization direction is again:

$$\delta = 2\frac{\pi}{\lambda}d(n_{TE} - n_{TM}) \tag{3.15}$$

where d is the grating thickness in light propagation direction. The phase retardation in Equation 3.15 is a function of the two effective refractive indices n_{TE} and n_{TM}. These indices depend on the grating depth d, its period Λ and its duty cycle d_c, which is the ratio between the period and the thickness of the grating ridge [22].

Q-plates

A metasurface q-plate transfers to the input beam an azimuthal phase-profile (OAM) with helicity sign depending on the input circular polarization [26]. This device can be realized through pure geometrical phase application. The metasurface can be both

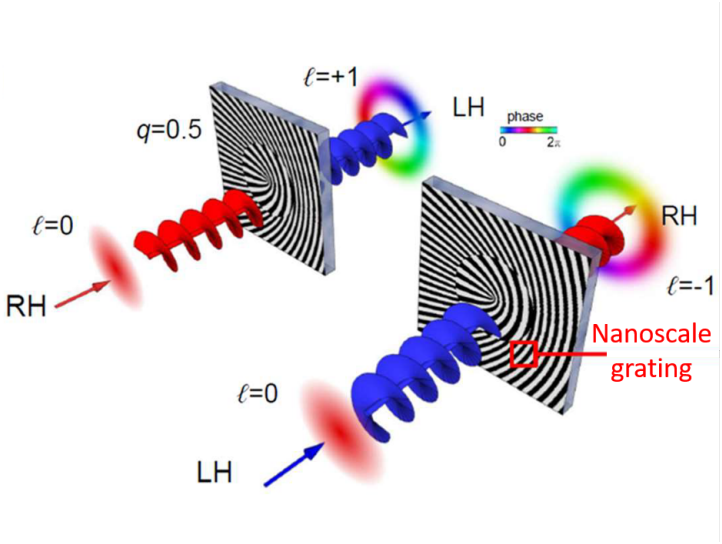

Figure 3.5: Q-plate realized with subwavelength grating. Scheme of the functioning: transformation of SAM beam into OAM beam with different topological charge l sign according to the sign of the input polarization. [26]

composed by meta-units or gratings. This device will be object of laser characterization in order to compare its OAM generation with the dual function metalens'.

Chapter 4

Lens design

A dual function metalens for the generation of an OAM beam, and for classical gaussian beam transmission is designed. All the metalenses features described in Section 3 are respected. The device is designed starting from its basic components, and then by building the overall lens structure.
The functions ϕ^+ and ϕ^- we want to be realized, respectively under LCP and RCP, are the generation of an OAM beam with $l = 1$, and the transmission of the incident gaussian beam:

$$\begin{aligned} \phi^+(x,y) &= e^{i\phi(x,y)} \\ \phi^-(x,y) &= e^{ic_o} \end{aligned} \tag{4.1}$$

The aim is, through the single meta-atom simulation, to realize a library of bi-refringent meta-atoms respecting the constraints given by:

$$\begin{aligned} \delta_x &= \frac{1}{2}(\phi^+(x,y) + \phi^-(x,y)) \\ \delta_y &= \frac{1}{2}(\phi^+(x,y) + \phi^-(x,y)) - \pi \end{aligned} \tag{4.2}$$

Which means that each single meta-atom must behave like a half-wave plate optical element. The library will collect this kind of units. Another key element for the selection of the meta-units is the transmission parameter of the meta-atom: the ratio between the incident intensity and transmitted intensity must be comparable for the orthogonal linear polarized modes, and its values close to 1. This is illustrated in Section 4.1

After the realization of this library, the lens is designed by locating the meta-atoms in

the correct position along its surface. Besides Equation 4.2, the pillars must respect the equation describing their orientation 3.14:

$$\theta = \frac{1}{4}(\phi^+(x,y) - \phi^-(x,y)) \tag{4.3}$$

This part of the design is reported in section 4.1.1.

Lastly, in this chapter, the simulation of the optical behaviour of the lens is performed for the LCP and RCP incident polarizations.

Before proceeding with the dual function lens, the first step was the design of single-function lenses, composed by the same meta-atom achieving the HWP condition, and used as a simple PBOE element. This device behaviour was explained in Section 3.1.2. These lenses are produced as a preliminary exercise for testing the home-made design and simulation softwares.

4.1 Meta atom simulation

The meta-atom constituting the basic unit of this lens was simulated using finite elements method with COMSOL software [27]. A parallelepiped pillar was positioned on a silica glass substrate and surrounded by air. The input port is positioned to match the lower face of the glass layer, while the output one corresponds to the top face of the air box. Periodic Floquet boundary conditions [28] on the transverse faces of the unit cell with respect to the direction of propagation of light were applied, and perfectly matched layer boundary conditions on the longitudinal faces, so that the ports act as absorbing surfaces and there is not an non-physical wave reflection in the z-direction inside the meta-unit. The cell was discretized with "fine" mesh option. A set of meta-atoms with different base shapes and dimensions for the pillar was simulated. [29]

Simulation of TE and TM illumination mode were separately carried out in order to investigate the unit's birefringence. The scattering parameter s_{21} was calculated: it represents the complex impedance between an output and input port. Scattering parameters (S-parameters) are complex-valued, frequency dependent matrices describing the transmission and reflection of electromagnetic waves at different ports of devices like filters, antennas, waveguide transitions, and transmission lines. S-parameters originate from transmission-line theory and are defined in terms of transmitted and reflected voltage waves. All ports are assumed to be connected to matched loads/feeds, that is, there

is no reflection directly at a port. For a device with n ports, the S-parameters are

$$S = \begin{bmatrix} S_{11} & S_{12} & .. & S_{1n} \\ S_{21} & S_{22} & .. & . \\ . & . & .. & . \\ . & . & .. & . \\ S_{n1} & S_{n2} & .. & S_{nn} \end{bmatrix} \tag{4.4}$$

where S11 is the voltage reflection coefficient at port 1, S21 is the voltage transmission coefficient from port 1 to port 2, and so on. The time average power reflection or transmission coefficients are obtained as $|S_{ij}|^2$. Hence the argument of the imaginary number s_{21} corresponds to the phase acquired by light passing through the atom [27]. The pillar geometry was set in order to have the output and input port at a distance, which makes legitimate the far-field approximation.

The pillar was simulated rectangular base and elliptical base shaped, with x and y sides and semi-axes respectively varying in ranges indicated in Table 4.1. Different shapes were simulated in order to have a wider library of pillars and being able to discretize regularly the phase range.

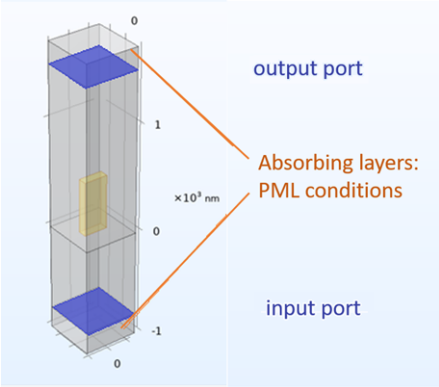

Figure 4.1: Structure of meta-atom simulated with COMSOL [27]

unit period	500 nm
pillar height	500 nm
air thickness	1500 nm
glass thickness	800 nm
absorber thickness	200 nm
x-pillar range	[60 : 320] nm
y-pillar range	[60 : 320] nm

Table 4.1: Meta-atom geometry parameters for COMSOL simulation

Thus, only pillars with phase difference of $\Delta\phi = \pi$ between TE and TM phaseshift were considered, with a tolerance on the phase difference of 5%. Among these, only those whose transmission parameter is similar in both modes are selected. In Figure 4.2 it is shown a graph that considers this set of 30 pillars and plots their transmitted phases and their displacement from half wave plate behaviour (in orange).

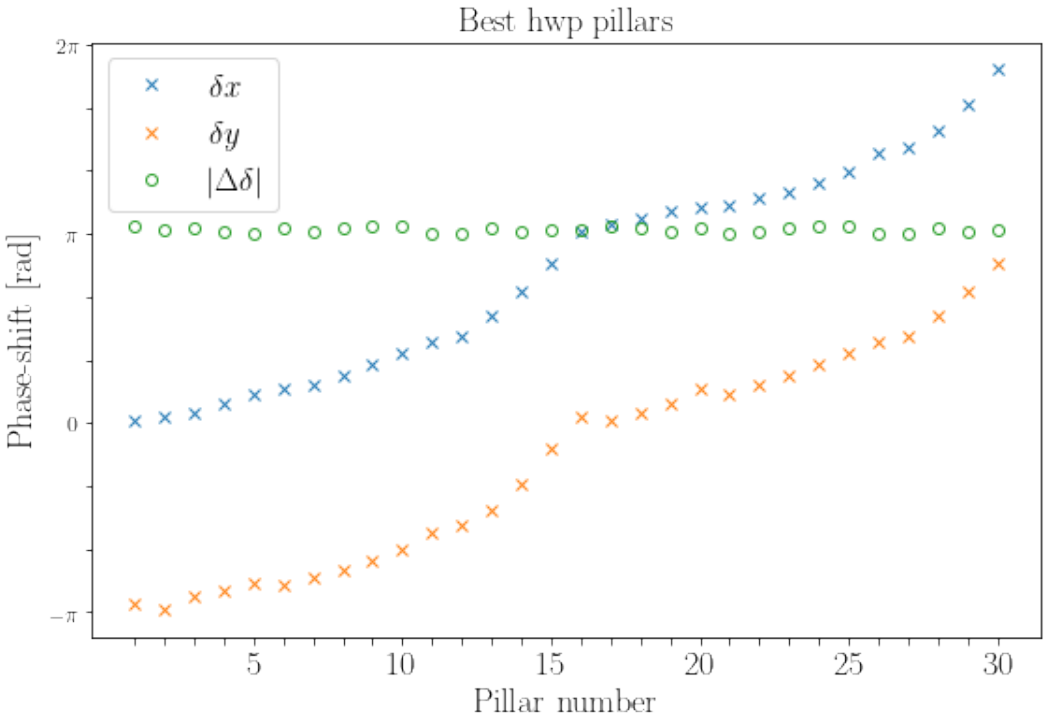

Figure 4.2: Set of pillars best approximating the half wave plate condition. In blue and orange the phase-shifts given by the pillars in mode TE and TM are shown. In green there is the absolute value of the difference between TE and TM difference and π. 30 pillars were considered, since they fulfilled the requirements.

4.1.1 Lens CAD writing

In the following, the dual function metalens is designed and the CAD file acting as an input for the lithography process is produced. This section is composed by the design process for different single-function metalenses, and ultimately by the project of the dual function, which is the real objective of the design process.

The metalens is discretized into metapixel regions, where each metapixel corresponds to a single meta-atom and has a side of 500 nm. The correct pillar size and orientation is chosen according to its in plane x-y position. The metapixel region is as well discretized with a matrix of zeros and ones, according to the drawing resolution needed. The matrix has value zero for the regions without the pillar and 1 for the region where the pillar is present. The pillar is placed in the centre of the pixel and then rotated, then its boundaries are identified. The lens is written in '.GDSII' format, thus each pillar is recorded as an element of type 'boundary'. The data file is then read with the software 'KLayout'.

Single-function lenses

In this case, the exploited phase is purely geometrical and the same meta-atom is used with different orientations on the lens surface; the efficiency phase conversion is obviously valid, so the pillar shape is chosen among the set of simulated meta-atoms working as half wave plates, reported in Figure 4.2 selecting the one with the highest efficiency. The dimensions of the selected meta-atom are $[130, 270]$ nm. Its simulated transmission efficiency is 99.7%.
In Figure 4.3 the central region of two lenses designed for producing an OAM beam with unitary charges $l = 1, 3$ respectively are showed. It is possible to see the pillar orientation and relate it to the local transmitted phase ($\theta(x, y) = 2\Omega(x, y)$): in fact in the lens with $l = 1$, following a circular path centered in the metalens, the pillar orientation complexively changes of π, in order to account for a total phase profile varying of 2π. An analogue argument can be discussed on the metalens with $l = 3$, where the orientation changes of 3π.

Dual function lenses

According to the desired phase discretization step $2\frac{\pi}{n_d}$ the pillars giving the phase-shift closest to the ideal one are chosen among this set of 30. The selection with lowest displacement from perfect discretization turned out to be the one showed in Table 4.2. It was chosen $n_d = 14$ since it allowed the best possible discretization of the range

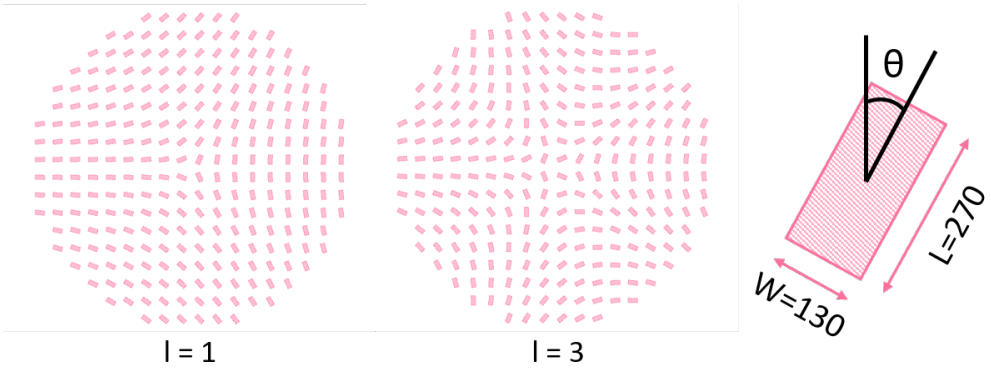

Figure 4.3: Central region of lenses realizing beams with OAM of l=1 and l=3. Representation of the pillar dimensions and orientation.

$[-pi : +pi]$. From the table it can be seen that the intervals $[0 : \pi]$ and $[-\pi : 0]$ are discretized by the same pillars with exchanged x and y base dimensions (the two portions of Table 4.2 report the pillars covering these phase intervals for TE polarization). The reason is that changing from phase TE to TM is equivalent to rotating of 90° the pillar, maintaining the same incoming polarization. So we expect the phase-shifts to differ of π in both cases. This leads to a descretization with 7 effective pillars.
In the process of lens writing, according to the two functions that the lens has to realize under opposite circularly polarized illuminations $\phi_R(x, y)$ and $\phi_L(x, y)$, the real desired phases δ_x and δ_y are discretized according to the chosen number of meta-atoms n_d and the pillar corresponding to the correct phase-shift is chosen for every metapixel.

Pillar	x [nm]	y [nm]	shape	Pillar	x [nm]	y [nm]	shape
1	190	90	r	8	90	190	r
2	130	270	r	9	270	130	r
3	130	240	r	10	240	130	r
4	130	220	r	11	220	130	r
5	220	150	e	12	150	220	e
6	130	170	r	13	170	130	r
7	120	170	r	14	170	120	r

Table 4.2: Table showing the dimensions of selected pillars. The numbers representing the pillars matches the ones in the x-axis of Figure 4.4. The shape is indicated with 'r' if the pillar base is rectangular and with 'e' if it is elliptical.

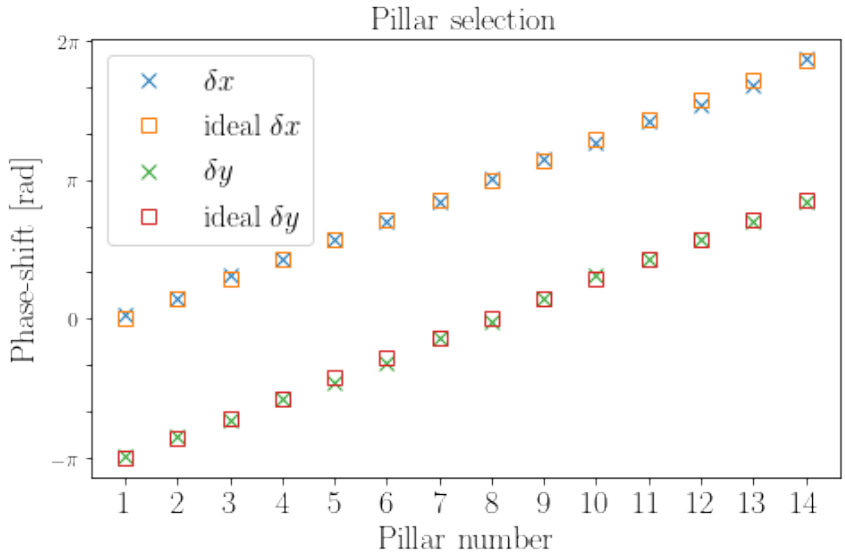

Figure 4.4: Pillars selected for the discretization of the $[-\pi, +\pi]$ interval with 14 pillars. In this plot the ideal and effective transmitted phase-shift are reported

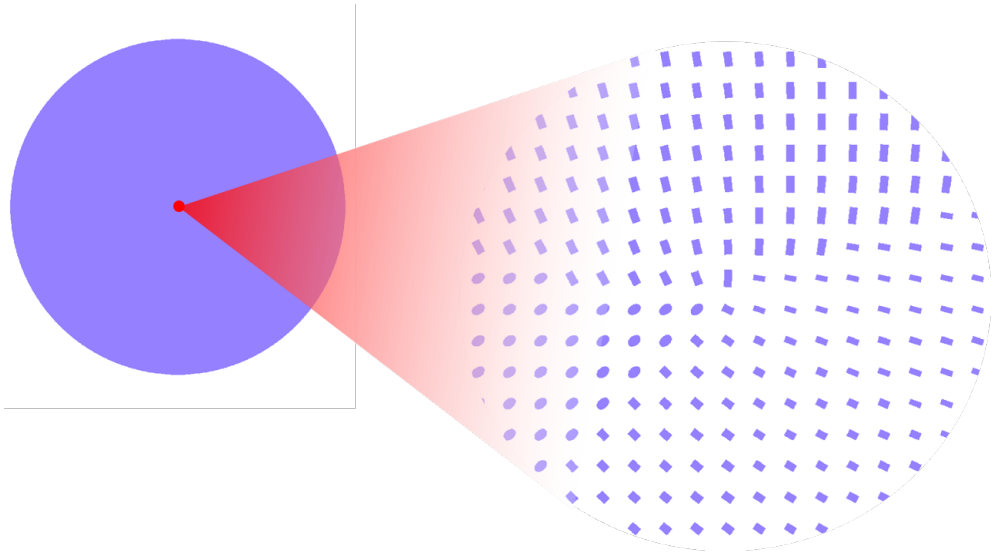

Figure 4.5: The designed lens with a diameter of 1 mm is shown with two magnifications. The pictures are set in the centre of the ML. In the magnified picture it is possible to see the pillars with different shapes and orientations.

4.1.2 Laser illumination simulation

In order to simulate the structuring of light due to the meta-atoms, a gaussian beam is simulated with the phase acquired due to the lens. This is done for the dual function metalens for both ideal case, in which the phase is perfectly uniformly discretized, and for the real case of the phase corresponding to the pillars, which has been previously simulated. The simulations were carried out considering a discretized phase transmitted by the lens point-wise for each meta-unit, and the electric field is discretized accordingly. A gaussian beam, whose beam waist is chosen to have the majority of intensity intersecting the patterned region of the lens, is considered. Its amplitude $u_0(x, y, z)$, where x,y and z are the discretized coordinates of the metapixel centers, is then point-wise multiplied by the phase value in each metapixel.

Then we need to evaluate the intensity profile as a function of the distance from the lens. According to paraxial Fresnel diffraction the diffraction field at a propagation distance z is:

$$\tilde{u}(R, z) = \frac{e^{i2\pi z/\lambda}}{\sqrt{i\lambda z}} \times \int u(r, 0) \exp\left(\frac{i\pi}{\lambda z}(R - r)^2\right) \, dr \tag{4.5}$$

which is nothing but the linear convolution of the input wave and the convolution kernel:

$$h(R, z) = \frac{e^{i2\pi z/\lambda}}{\sqrt{i\lambda z}} \exp\left(\frac{i\pi R^2}{\lambda z}\right) \tag{4.6}$$

so that

$$\tilde{u}(R) = \int u(r) h(R - r) dr \tag{4.7}$$

where r and R are both spatial coordinates, used to indicate the spatial locations of the signal before and after the propagation. [30]

The Fourier transform of h(R,z) is:

$$H(k_\perp, z) = \frac{\exp(i2\pi z/\lambda)}{\sqrt{i\lambda z}} \exp(-i\pi\lambda z k_\perp^2) \tag{4.8}$$

where f_X is the spatial frequency. [30]

Equation 4.5 can be solved in two mathematically equivalent ways: Fresnel Transfer Function Method (Fres-TF) and Fresnel Impulse Response Method (Fres-IR). In Fres-TF, the transfer function is directly sampled by $H(f_X)$, while in Fres-IR, the transfer function is obtained as the Fourier transform of the sampled h(X). The reason for this

distinction are the ranges of applicability of the two methods, which are almost complementary. According to the sampling theorem, for avoiding sampling aliasing for Fres-TF we get:

$$z \leq \frac{2N\Delta_x^2}{\lambda} = p_C, \tag{4.9}$$

which means that H can be correctly sampled only in this range, while for Fres-IR:

$$z \geq \frac{2N\Delta_x^2}{\lambda} = p_C, \tag{4.10}$$

so that in this (almost) complementary range we have to sample h. [30]

To sum up:

- Check p_C:
  1. If $z \leq p_C$: Sample $H(k_\perp, z)$ in frequency domain
  2. If $z > p_C$: Sample h(R, z) in length domain
- Calculate $A(k_\perp, z)$, respectively defined as:
  1. $A(k_\perp, z)$=FFT$[U(R,0)] \cdot H(k_\perp, z)$
  2. $A(k_\perp, z)$=FFT$[U(R,0)] \cdot$ FFT$[h(R,z)]$
- The diffraction field is equal to the Inverse Fast Fourier Trasform of A: $U(R,z) =$ IFFT$[A(k_\perp, z)]$

Single-function lenses

The single function lenses optical behaviour was simulated as a first test for the simulation algorithm. The function considered is the transmission of an OAM phase profile:

$$\phi = e^{il\varphi} = l \cdot \arctan\left(\frac{y}{x}\right) \tag{4.11}$$

with $l = +1, -1, +2, +3$. This was done in order to investigate the intensity- and phase-map of OAM beams with different unit charge values.
In Figure 4.6 the transverse intensity profiles at $z = 1$ mm are shown in the upper row; they match the theoretical doughnut distributions for the OAM. In the second row it is possible to see the number of phase lobes starting from the centre. This number, as expected, corresponds to the topological charge l value. The spiral is oriented according to the positive or negative sign of l. This can be seen clearly by comparing the first and the second picture in figure 4.6, for $l = \pm 1$.

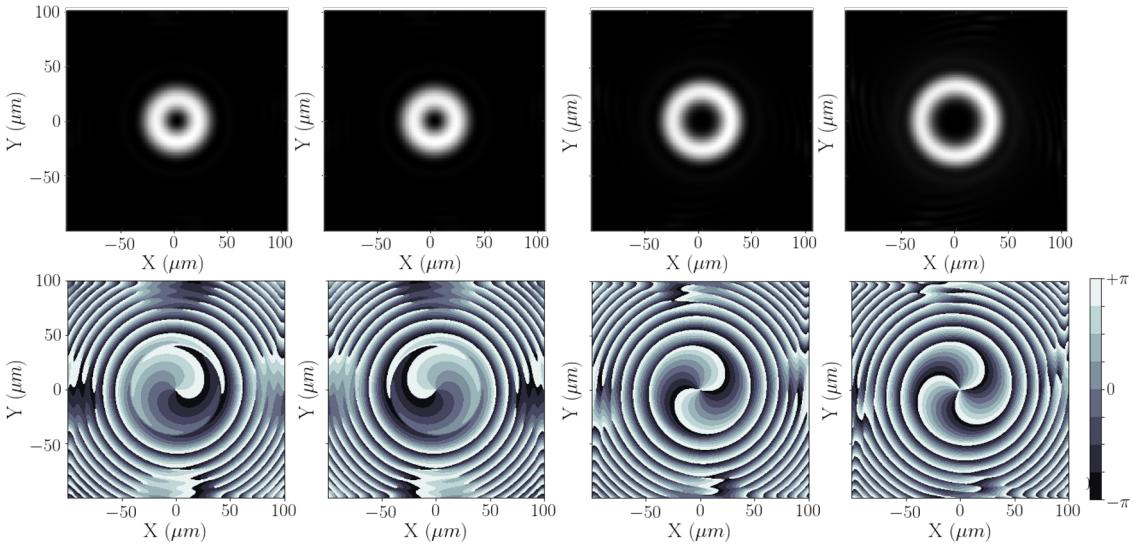

Figure 4.6: Simulation of the intensity and phase profile of OAM beams with $l = +1, -1, +2, +3$ at a distance of $z = 1$ mm from the metalens.

Dual function lens for generation of OAM and gaussian beam

The function considered for the metalens are: the generation of an OAM beam of charge $l = 1$ for LCP, and the addiction of a uniform phase c_0 to the gaussian beam (this does not alter its equal-phase surfaces) for RCP.

$$\Phi_{\mathrm{OAM}}(x, y) = l \arctan\left(\frac{y}{x}\right) \tag{4.12}$$

$$\Phi_{const}(x, y) = c_0 \tag{4.13}$$

The first simulation (Figure 4.7) considers the phase interval uniformly discretized, while the second simulation (Figure 4.9) uses the phases resulting from the meta-atom simulation, which thus have a slight displacement from the ideal discretization. The simulations show the beam from a side view in the top plots and from a tranverse point of view, at different distances from the metalens, in the bottom plots. The outcome of the simulation with the simulated phase discretization turned out to be very similar to the ideal one.
Since the phase profile plays a crucial role in the definition of these waves, and in their difference, in Figure 4.8 and 4.10 the phase profile simulated for the gaussian and OAM function at 1 mm distance from the metasurface are represented. It is possible to appreciate the helicoidal phase-profile of the OAM beam with $l = 1$ and the gaussian phase-front, which maintains a constant value in the center of the beam. The phase plots suffer of border-effects, since the beam waist size is comparable to the metalens size, which was simulated with a diameter of 200μm due to high computational cost. For reducing at least the writing time for the lens file, it is possible to consider the same metalens portion and add a padding on the borders of the lens phasemap, in order to avoid the intraction with the border.

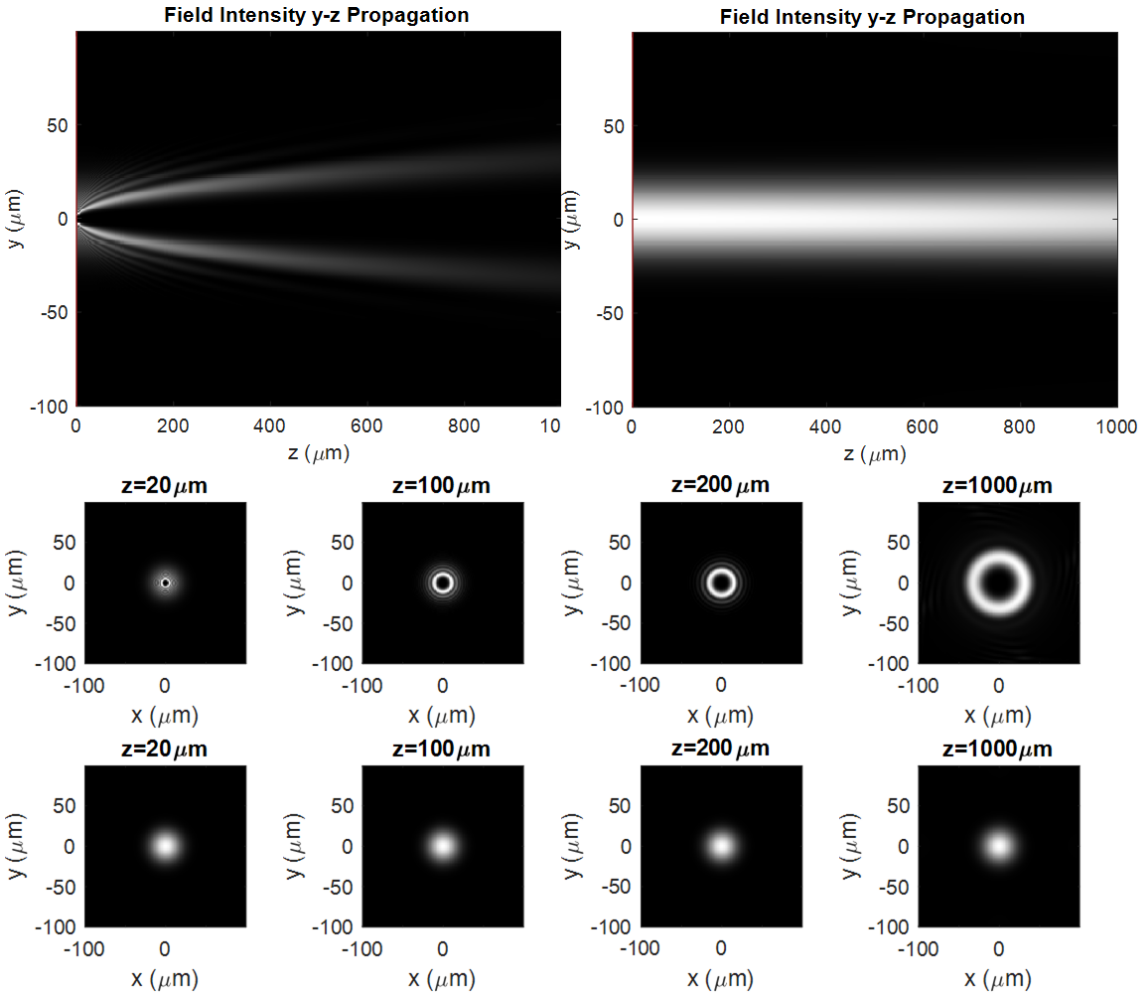

Figure 4.7: Simulation of the metalens whose functions are OAM with $l = 1$ and gaussian beam. The simulation is carried out with a perfect phase discretization.

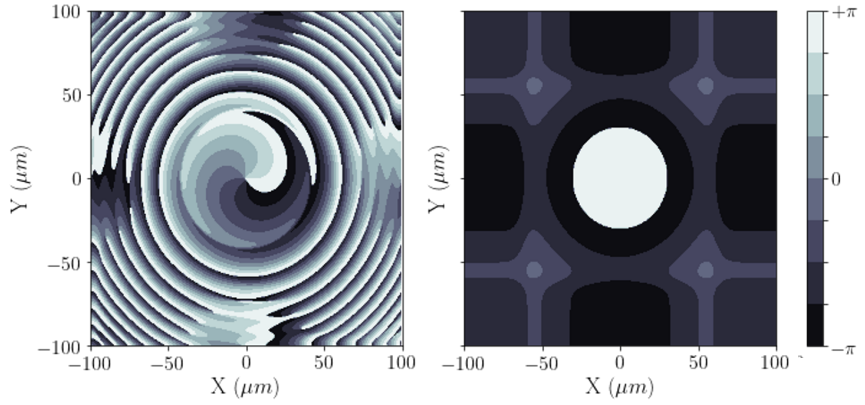

Figure 4.8: Phase-maps of the two functions (ideal discretization).

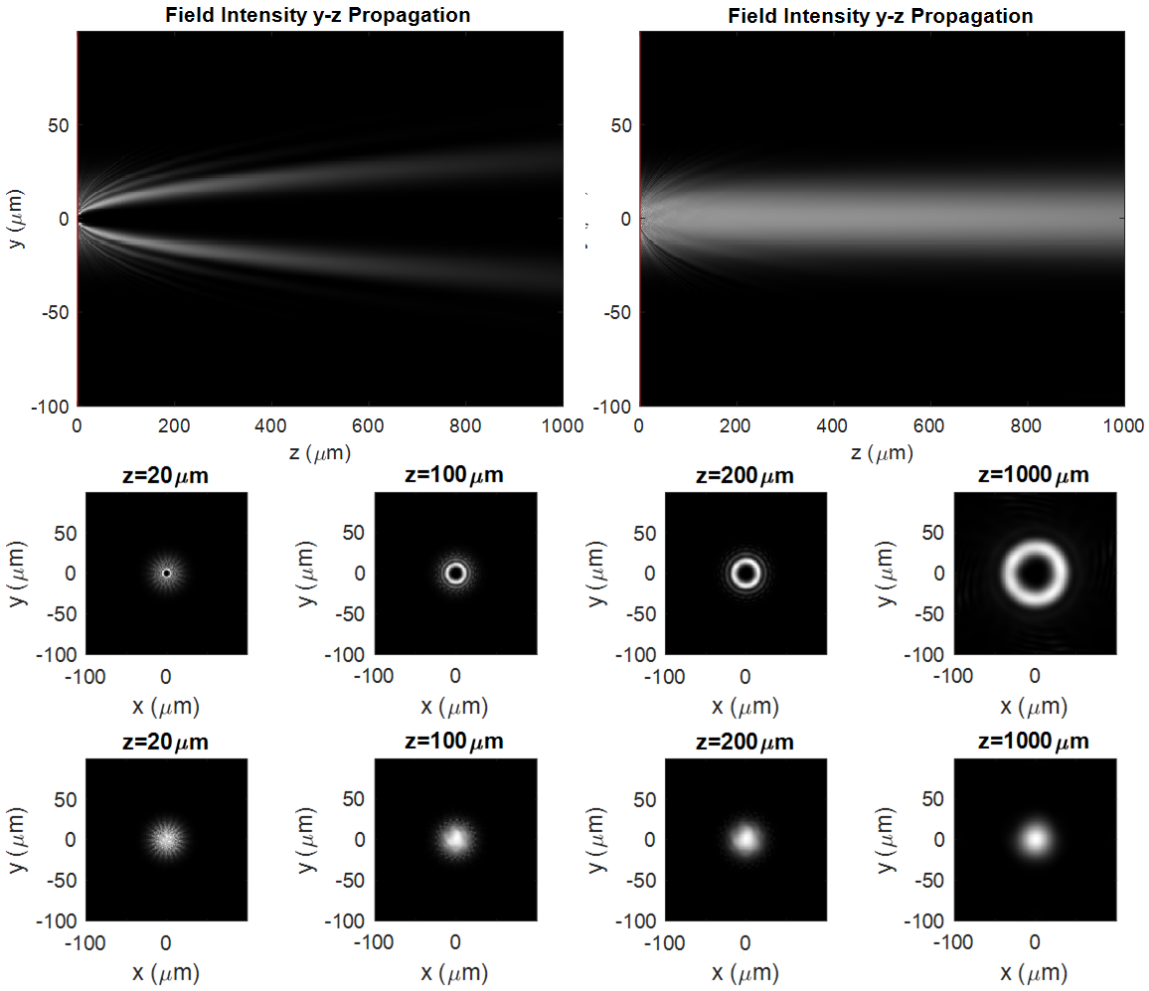

Figure 4.9: Simulation of the metalens whose functions are OAM with $l = 1$ and gaussian beam. The simulation is carried out with the simulated phase discretization.

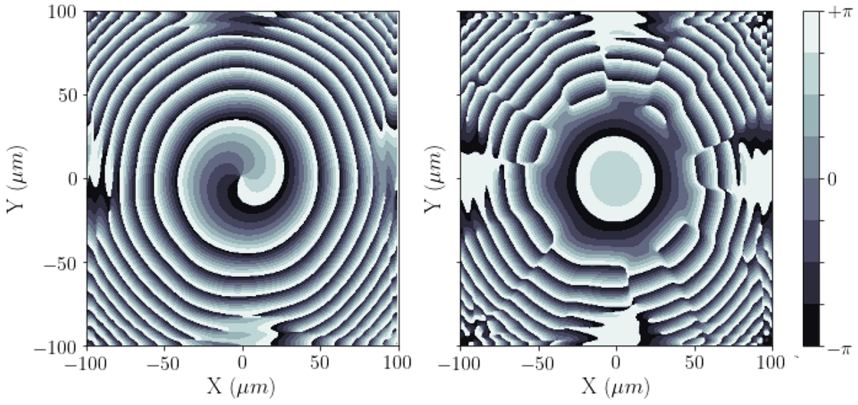

Figure 4.10: Phase-maps of the two functions (real discretization).

Metalenses projet for fabrication

The metalenses that are fabricated (5.2) rely on a design which comes from the optimization of the process explained above. The final set of pillars has different geometric features, but realizes the same function. The considered meta-atoms have a dimension of 400×400 nm and the pillar set is composed by $n_d = 12$ pillars with the dimensions reported in Table 4.3. The simulation of the metalens with real phase discretization is showed in Figure 4.11. The simulation result is very similar.

Pillar	x[nm]	y[nm]	shape
1	280	130	r
2	80	280	e
4	120	190	r
5	150	220	e
6	130	240	r
7	130	280	r
8	220	80	r
9	200	100	r
10	190	120	r
11	220	150	r
12	240	130	r

Table 4.3: Pillar set used for the design of the fabricated metalens.

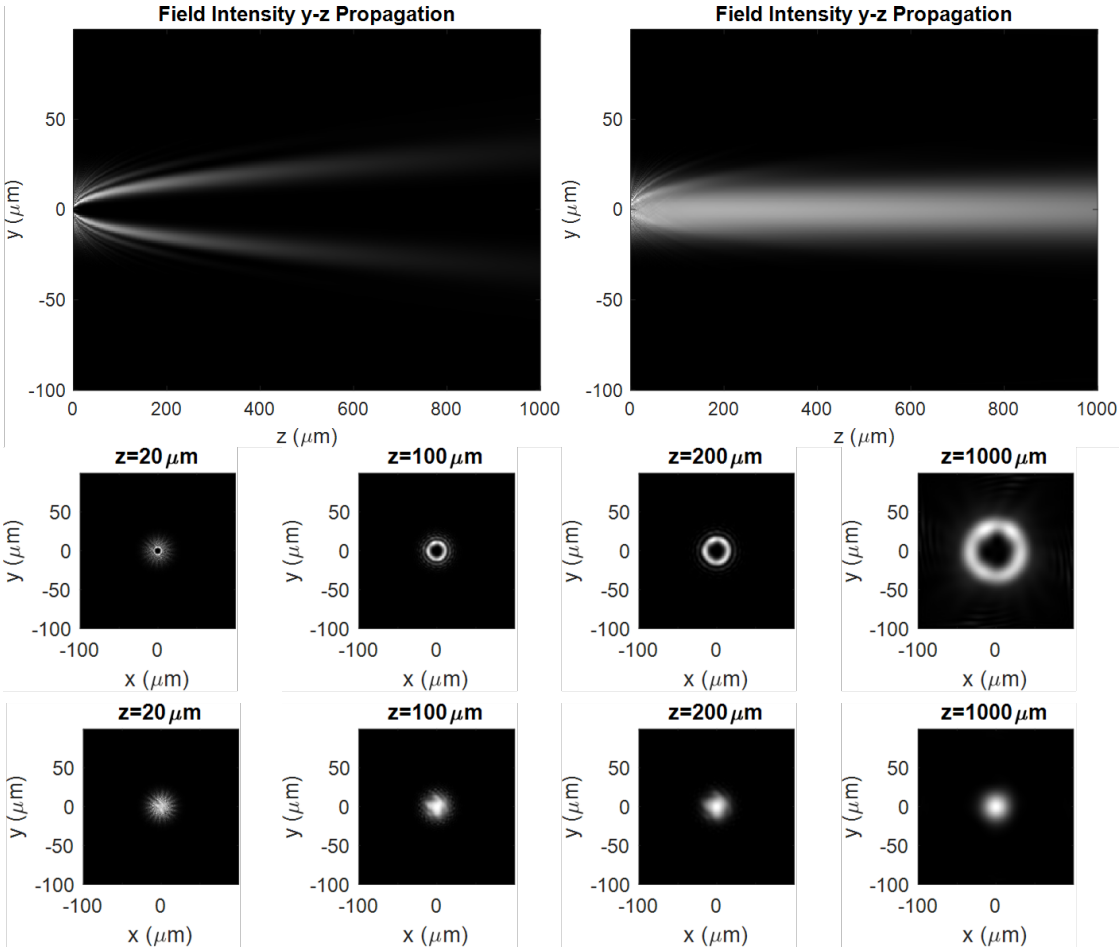

Figure 4.11: Simulation of dual function lens with the design applied to fabrication.

Chapter 5

Fabrication

5.1 Nanoimprint lithography

This thesis work is based on the nanofabrication technique of the nanoimprintg lithography (NIL). In the following section, the main features of NIL will be resumed.

The Nanoimprint lithography is a method of fabricating micro/nanometer scale patterns with low cost, high throughput and high resolution [31]. Unlike traditional optical lithographic approaches, which create pattern through the use of photons or electrons to modify the chemical and physical properties of the resist, NIL relies on direct mechanical deformation of the resist and can therefore achieve resolutions which are not affected by diffraction limited focusing, in case of optical lithography, or electron beam scattering, in case of electron beam lithography [32]. The resolution of NIL mainly depends on the minimum template feature size that can be fabricated for the master. In addition, nanometer sized patterns can easily be formed on various substrates, e.g., silicon wafers, glass plates, flexible polymer films, and even nonplanar substrates. [33]

NIL has two steps: **imprint** and **pattern-transfer**. In the imprint, a patterned master is used to deform a thin resist film deposited on a substrate. In the pattern-transfer process, an anisotropic etching process, such as reactive ion etching, is used to remove the residual resist layer in the compressed area, and then the nanostructure is transferred to the substrate [34]. This process does not create a sample identical to the master, but the nanoimprinting inverts the structure tone.

The resist can be either a thermal plastic or a UV curable polymer or other deformable materials. For a thermal plastic resist, the polymer is heated above its glass transition

temperature, T_g , to obtain a melt with the desired flow properties [34]. The imprinting phase is realized following the steps below, with temperature and pressure transients showed in Figure 5.1:

- Heat stamp and substrate up to T_1, to soften thermoplast.
- Apply an imprint force or pressure P_1.
- Wait for polymer to flow into the mould cavities.
- Cool down to room temperature (below T_g) with imprint pressure applied.
- Release imprint pressure, when resist has hardened, to have a neat separation between the parts.

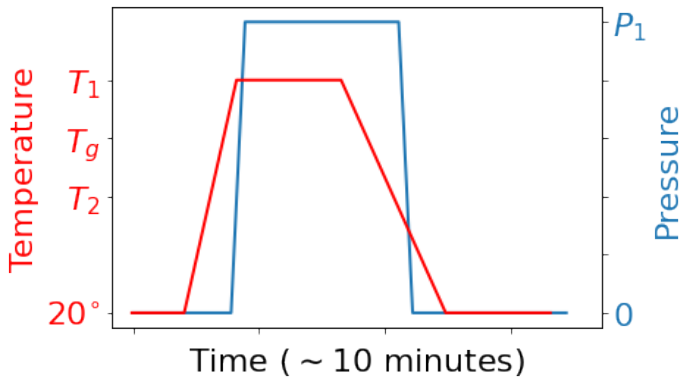

Figure 5.1: Plot of the pressure and temperature trend during the imprint time. The optimal parameters indicated in the y-axes are: $T_1 \sim T_g + 80°C$, $T_2 \sim T_g - 20°C$, $P_1 \sim 100 - 1000$ kPa.

The imprinting process can be modelled as an incompressible, viscous fluid of viscosity η_0 positioned between two parallel disks at initial distance $2h_0$, which decreases with time, as the disks approximate. The **Stefan equation** is a steady state solution that expresses the intensity of the force $\vec{F}$ needed, as a function of the disks motion ($\pm\partial h/\partial t$) and the disk radius R (Figure 5.2).

$$F = -\frac{3\pi R^4}{2h(t)^3}\frac{\partial h}{\partial t}\eta_0 \tag{5.1}$$

There is a strong dependence from the structure radius ($\sim R^4$), which means that large pattern features require a very intense force to be imprinted. The factor $\sim 1/h(t)^3$ indicates the difficulty of patterning resist layers with small thickness. This is relatable to the fact that the fluid must move inside the space between two walls very close to each other, and at each wall the flux is zero, as modelled by the no slip boundary condition.

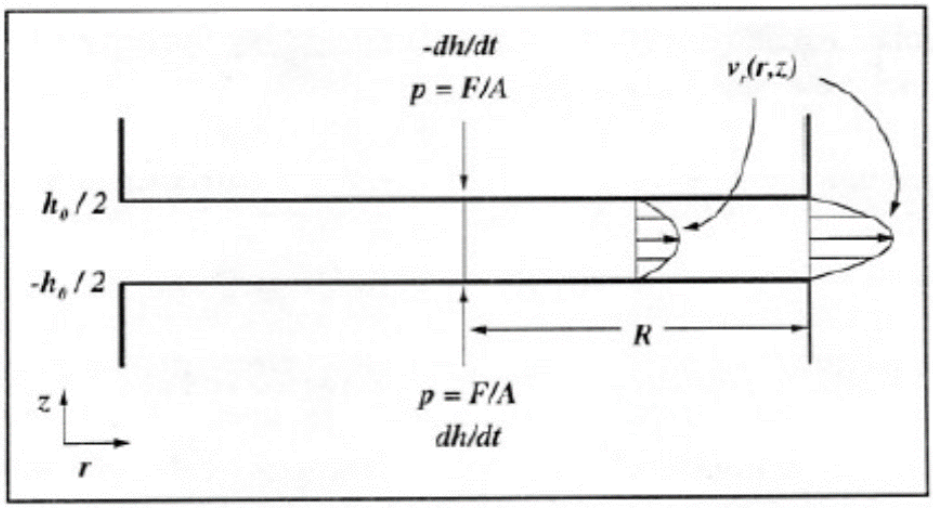

Figure 5.2: Scheme of moving disks which transmit the motion to the fluid in between them and representation of velocity profile [34].

Equation 5.1 has a linear dependence with viscosity, anyway η_0 greatly increases with increasing temperature.
The flow of the fluid results from the transfer of the disks motion, which is transferred into a radial flow of the fluid, $\nu_r(r, z)$ (Equation 5.2), from the disk centre outwards to its circumference [34]. The velocity profile of this flux is the one of a classical laminar flux with boundary conditions, thus the velocity dependence in z is parabolic, with maximum intensity at equal distance between the disks:

$$\nu_r(r, z) = -\frac{3}{4}\frac{\partial h}{\partial t} r \left[1 - \left(\frac{z}{h_0}\right)^2\right] \tag{5.2}$$

Residual layer

After the creation of the structures in the resist, they can be transferred to the transfer layer, i.e. the layer we want to pattern eventually. This is done through reactive ion etching (RIE) procedure. This procedure is illustrated in Section 5.1.2.
Before etching, we need to take care about the residual layer, as a layer of unpatterned resist remains above the substrate after the imprinting. As highlighted by Stefan equation, with the reducing of h(t), the force needed for the imprinting diverges. The final

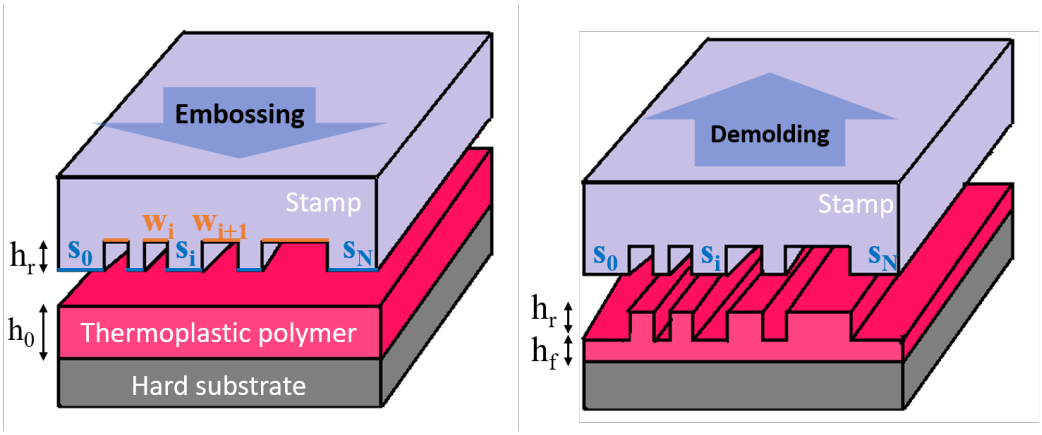

Figure 5.3: Imprinting procedure with pattern and resist features leading to the resist volume conservation through the embossing and demolding procedures. In this image a mono-dimensional patterning is considered. Adapted from [34].

RIE step can remove also the residual layer, but, since the RIE process is indiscriminative, it etches both the residual and the imprinted polymer pattern structure, resulting in pattern damage and distortion when it is excessive. So residual layer must be removed before etching, in our case dry etch in O_2 plasma is used.
Being the resist layer thickness a crucial quantity, it can be calculated in advance, by knowing the pattern filling factor, and deciding the final height of residual layer h_f. In fact, resist polymer is not compressible, thus volume conservation applies: The initial resist thickness h_0 can be calculated as follows in Equation 5.3:

$$h_0 = (h_f + (1 - f_r)h_r) \tag{5.3}$$

where f_r is the ratio between the entire patterned area of the mould, and the area of the outstanding structures. This equation comes from the volume conservation of the polymer V_p:

$$V_p = h_0 \cdot A = (h_f + (1 - f_r)h_r) \cdot A \tag{5.4}$$

Too thin h_0 increases mold wear and damage. Too thick residual layer makes subsequent RIE more demanding: it is hard to control the pattern profile, as it is subjected to size shrinkage and the resulting structure will not have sides orthogonal to the substrates (tapered profiles). Besides, this kind of shape makes an eventual lift-off procedure almost impossible. Here comes the importance of the resist film thickness choice.

5.1.1 Pulsed NIL

A novel NIL technique was developed by Thunder-NIL s.r.l., called Pulsed-NIL, which allows to produce nanostructures in extremely short times. On the contrary, thermal-NIL is very time-consuming and the heat diffuses to areas surrounding that in which the pattern needs to be imprinted, causes the relaxation ("polymer reflow") of the previously imprinted nanostructures. Thanks to a thin conductive layer buried a few µm beneath the patterned surface of the stamp, the heat needed to perform the NIL process is delivered by the stamp itself by dissipating the energy of a short $(10 - 100\mu s)$ intense current pulse injected in the stamp and flowing uniformly below its surface while the pressure is applied. The generated heat quickly raises the surface temperature, typically ranging between 400 and $800°C$, causing the sudden melting of the thermoplastic material in contact with the stamp with the great increasing of its viscosity [35] [36].

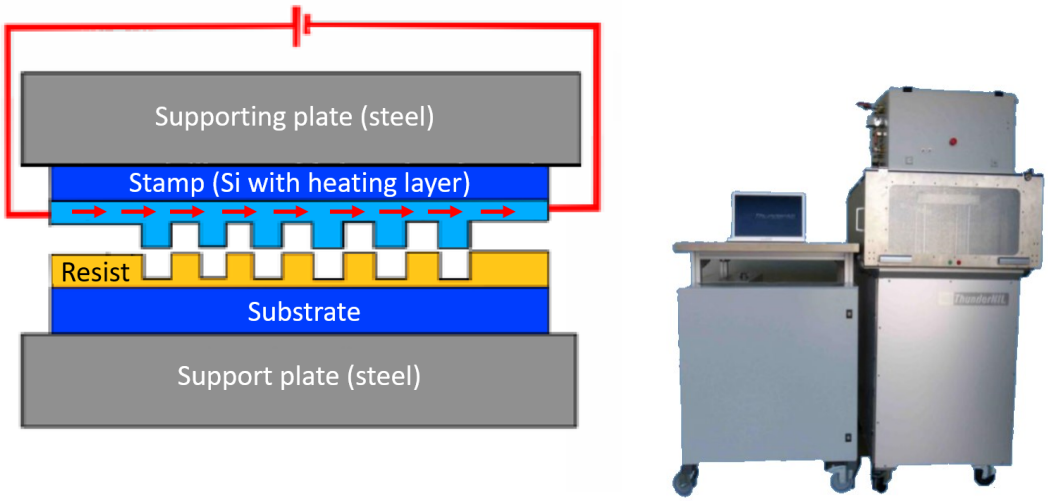

Figure 5.4: Scheme of thunder-NIL functioning and picture of Thunder-NIL machine. [35]

5.1.2 Pattern transfer process

The etching of the substrate is fundamental for transferring the pattern, obtained in the resist by the imprinting, to the substrate. The techniques used for this work are capacitively coupled plasma reactive ion etching and inductively coupled plasma reactive ion etching.
Reactive Ion etching (RIE) uses a plasma, which chemically reacts with a surface to remove material deposited on it. The plasma state describes a condition where one or more gases are held at a certain pressure and submitted to an electrical potential, caus-

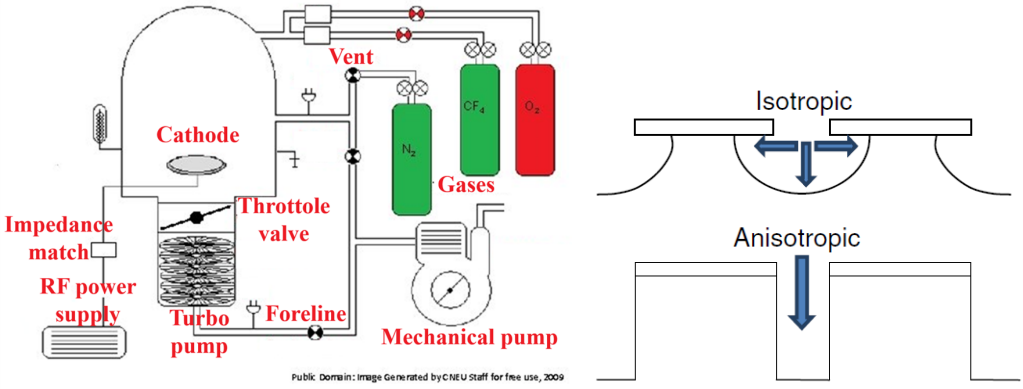

Figure 5.5: Scheme of RIE [40] and representation of isotropic and anisotropic etching [38].

ing the partial ionization of the gas atoms [37].
For CCP-RIE, the feed gas is injected directly in the vacuum chamber, between two parallel electrodes while the pressure reaches a certain level. The pressure is kept constant by keeping active the pumping system, with the valve for the high vacuum partially open, not to remove all the gas necessary for the plasma. Between the electrodes there is a DC bias, whose value depends on pressure and gas flow. Then a radio frequency (RF) voltage of 13.56 MHz is applied between the electrodes and the feed gas is ionized. Thus ions are accelerated by the DC bias until hitting the lower electrode, where the sample is places. This ion energy is essential in activating the etching process, since it is crucial for the reaction directionality (5.5), from which the good etching outcome depends, but it can also damage the structure if not appropriately calibrated [38]. In this process DC and RF voltages are not independent.
In the case of inductively coupled plasma (ICP) RIE, the gas alimenting the plasma is ionized remotely, through inductive coupling between the RF source and an antenna, positioned in the chamber, which causes the electron energizing. Electrons ionize the gas molecules and atoms at low pressure. The DC generator, instead, acts between the electrodes and is independent on the radiofrequency applied. [39]
This is the main factor resulting in a noticeably lowvoltage across all plasma sheaths at electrodes and walls. For instance, increasing ICP power would lead to higher plasma density and simultaneously to lower dc bias. Therefore, ICP reactors are capable of achieving anisotropic etching at a much higher rate than CCP reactors [38].

5.2 Dual-function metalenses fabrication

The procedure for the fabrication of dual function metalenses devices consists in the replica of a silicon master produced with Electron Beam Lithography (EBL) technique. The replica samples are made of a glass substrate, while the pattern is reproduced in a layer of amorphous silicon of the designed thickness. The fundamental fabrication steps are: the Nano-Imprinting Lithography (NIL) on a coating resist, the stripping of the residual layer, a chrome mask deposition, a lift-off process and silicon etching with Inductively Coupled Plasma Reactive Ion Etching (ICP RIE). The steps of the fabrication recipy are resumed in Figure 5.6.

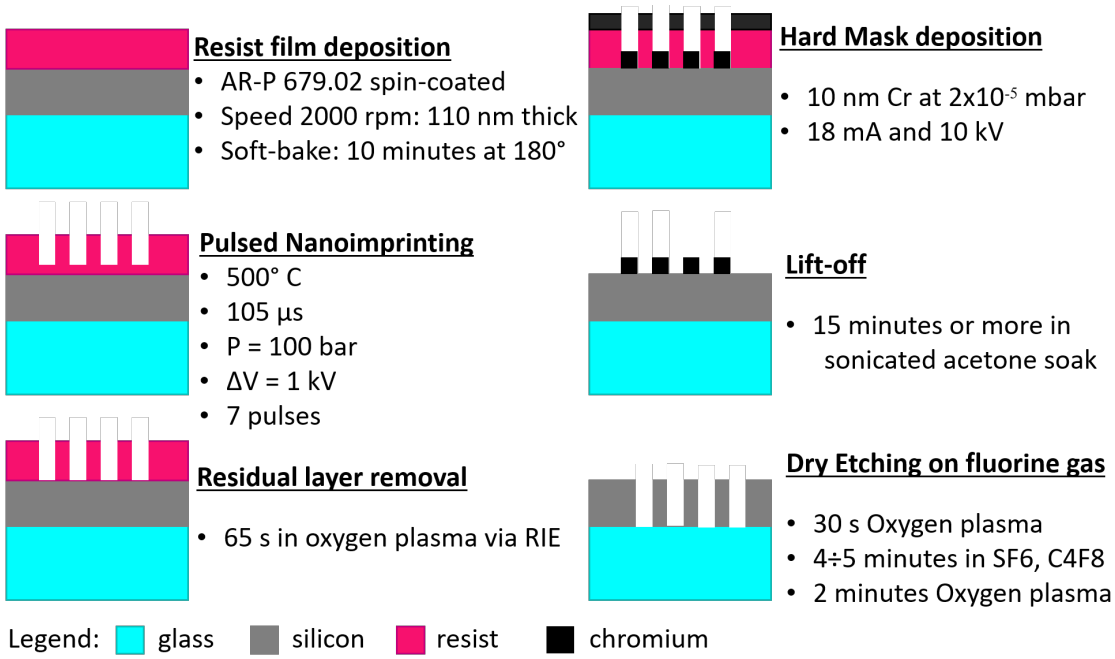

Figure 5.6: Details of the nanofabrication process. The steps show how the pattern of the master is transferred to the silicon layer of the samples.

Glass silicon samples preparation

Since the metalenses work at a wavelength in the visible light spectrum, the substrate must minimize light absorption at that wavelength. As substrate, borosilicate ($12\%B_2O_3 + 80\%SiO_2$) was used, as it provides minimal absorption loss in the visible range, and it is suitable for a dielectric amorphous silicon (a-Si) layer sputter-deposition. Glass slides were cut into portions small enough to not exceed the master size. The chosen dimensions are 25 x 25 mm. Glass was carved with a diamond tip, and then broken

according to the incision. The obtained samples were then washed with an RCA solution ($H2O : H2O2 : NH4OH = 3 : 1 : 1$); RCA is used for cleaning wafers and in particular removing organic deposits on the surface. The samples were immersed into the solution in a glass baker and warmed up to 65° for 30 minutes under fume hood.

Then a layer of amorphous silicon (a-Si) was magnetron-sputtered on the glass slides. The procedure is made of three steps:

- Argon oxygen plasma cleaning for 5 minutes.
- Silicon presputtering for cleaning the target: the silicon is preliminary sputtered on a lid in order to clean the sputtering target from contaminating agents.
- Silicon sputtering on the samples: 58 minutes for obtaining a 510 nm thick layer of silicon. The sputtering is performed using a radiofrequency during the process.

Since the meta-atoms designed have a height of 500 nm, the silicon was sputtered with a thickness of 510 nm, in order to account for the error in the etching time. The AR-P679.02 resist was then spinned on the samples: the samples were initially cleaned with acetone and isopropanol. The resist was spinned at 2000 rpm for obtaining a thickness of 100 nm, which is the tabulated thickness for this spinning velocity. Then it is baked on a hotplate at 180° for 10 minutes. This resist belongs to the family of PMMA resists, which are composed of poly(meth)acrylates with different molecular masses. The glass temperature of PMMA layers is in the range of 105° C, and polymers are thermostable up to a temperature of 230° C.

Master preparation

The lithographic realization of the master was commissioned in a third-party laboratory with the following procedure.
A JBX-6300FS JEOL EBL machine, 12 MHz, 5 nm lithographic resolution, working at 100 kV with a current of 100 pA was used. [22]. A 280 nm layer of AR-N 7720.30 resist (Allresist GmbH) was spun on a customized silicon substrate. An exposition dose of 325 $\mu C/cm^2$ was chosen from a previous dose matrix analysis. The resist pattern was transferred into the silicon substrate by means of STS MESC MULTIPLEX RIE plasma etching in configuration working at 13.56 MHz frequency.

The master was cleaned with an Oxygen plasma in a vacuum chamber located in a clean room. The O_2 flux was performed at a pressure of $4.6 \cdot 10^{-4}$ mBar with a voltage drop of 100 V and a radiofrequency of 13.56 MHz. The master was then analyzed with a

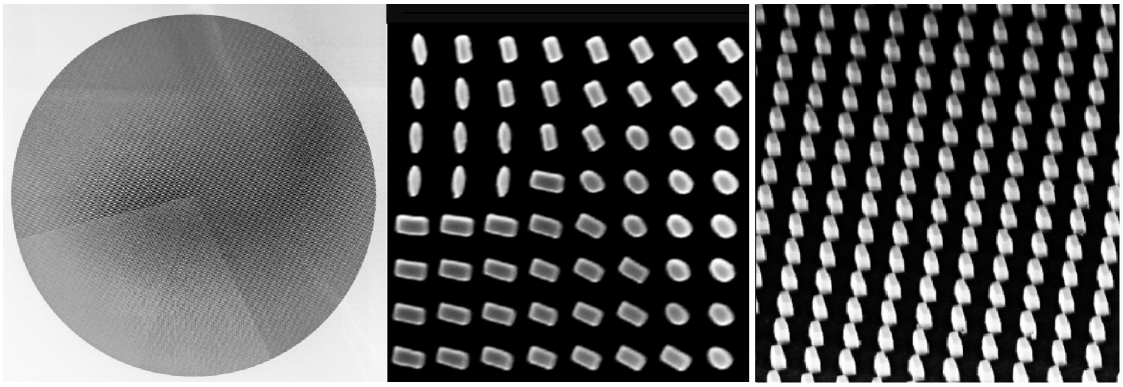

Figure 5.7: SEM images of the entire metalens (left), of the center of the metalens (centre) and of one zoomed portion of the metalens with 45° tilting (right).

Scanning Electron Microscope (SEM), images are reported in Figure 5.7. It was then cleaned in pirana, which is a mixture of sulphuric acid (H_2SO_4), water (H_2O), and hydrogen peroxide (H_2O_2), used to clean organic residues off substrates. The pattern generated by EBL was transformed into a master stamp after an overnight silanization process with Trichloro(1H,1H,2H,2H-perfluorooctyl)-silane PFOTS; silanization is the covering of a surface with organofunctional alkoxysilane molecules, which makes the surface hydrophobic.

Then the master was prepared for the Pulsed NIL process with Thunder NIL machine on the glass silicon slides. The master must be in electrical contact with the high voltage source for the imprinting. Two portions of the master near the edges were sputtered with a metallic layer and then brazed with copper sheets, which connect it to the circuit of the Thunder NIL. The master was realized with doped silicon, in order to allow current flow.

Imprinting

The replica process was conducted using a pulsed NIL press with heating/cooling plates, called ULISS [35], its functioning is explained in Section 5.1.1. The imprinting process was realized with 7 subsequent impulses in order to maximize the pattern transfer. The outcome of the lithography was then checked with an optical microscope. Its resolution did not allow to see the pillar structure, but the presence of the pattern was clearly distinguishable.

Residual layer removal

The removal of residual layer was performed in O_2 plasma with RIE. A different etching time was applied on three different samples in order to optimize this step of the process. The outcome was verified with optical microscope, which allows to see if the pattern has undergone damages. The chosen durations were: $55, 60, 65$ s. The best duration turned out to be 65 s. This fabrication parameter was applied to all the subsequent samples.

The key actions to do in order to use the RIE machine are:

- Close the chamber containing samples
- Open the vacuum pump
- Set throttole valve at 20%
- Open gas flow inside the chamber
- Wait for the reaching of required pressure for a voltege bias of $100V$ when activating the radiofrequency
- Activate the radiofrequency for the desired etching time
- Stop radiofrequency and close gas inlet and gas line
- Open throttole valve
- Stop vacuum pump
- Vent the chamber and extract the samples

Chromium mask deposition

A layer of 10 nm of chromium has to be deposited on the pattern. The mask must cover only the top of the patterned structure and their base, without covering the vertical sides. This is crucial for the outcoming of the lift-off process, thus, the directionality of the deposition is very important. The most appropriate machine for this work is metal evaporator, but, because of its unavailability, the process was performed with Magnetron sputtering, with an analogue procedure to the one for a-Si sputtering on the glass samples. The sputtering process lasted 14 s.

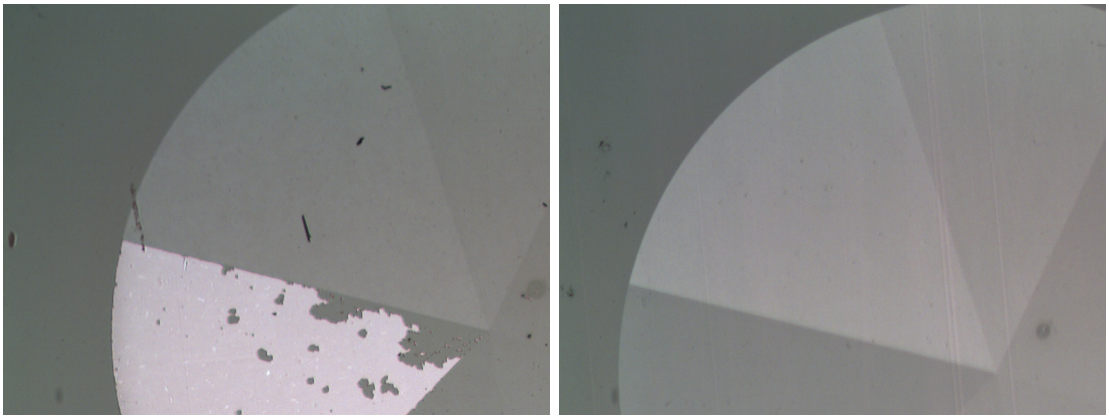

Figure 5.8: Example of one sample with problematic and one sample with successful liftoff in the same metalens region.

Lift-off

After the imprinting the samples present a pattern with negative tone, covered with a chromium hard mask. The lift-off procedure allows to change the tone of the pattern. This is done by removing the resist structures, which are dissolved in acetone. The metal layer covering the resist is removed as well, while the chromium deposited directly on the substrate is not in contact with the resist, thus it is selectively conserved. The lift-off is successful if the metal deposition is anisotropic and the vertical sides of the resist structures are not covered in metal. Otherwise the resist is not be reached by the reactant and hence is not dissolved. The patterned metal, in our case chromium, functions as a mask for the successive pattern transfer into amorphous silicon layer.
The lift-off was done with an acetone soak and introducing the baker in a sonicator. The procedure lasted about 30 minutes. The result of lift-off was periodically checked with an optical microscope. For some samples, the lift-off did not succeed in certain regions of the pattern, where there are clear chromium leftovers. This probably happened because the mask was not perfectly deposited, but had covered also the vertical sides of the pattern, the different results can be seen in Figure 5.8.

Etching

At this point, the samples are composed by the unpatterned a-Si transfer layer covered with a Chromium mask with the positively toned pattern. This mask allows etching for several hundreds of nanometers. The etching is performed with ICP-RIE machine with a type of etching on fluorine gas (SF6, C4F8). The etching is performed on different samples with different duration, which means the reaching of different heights for the

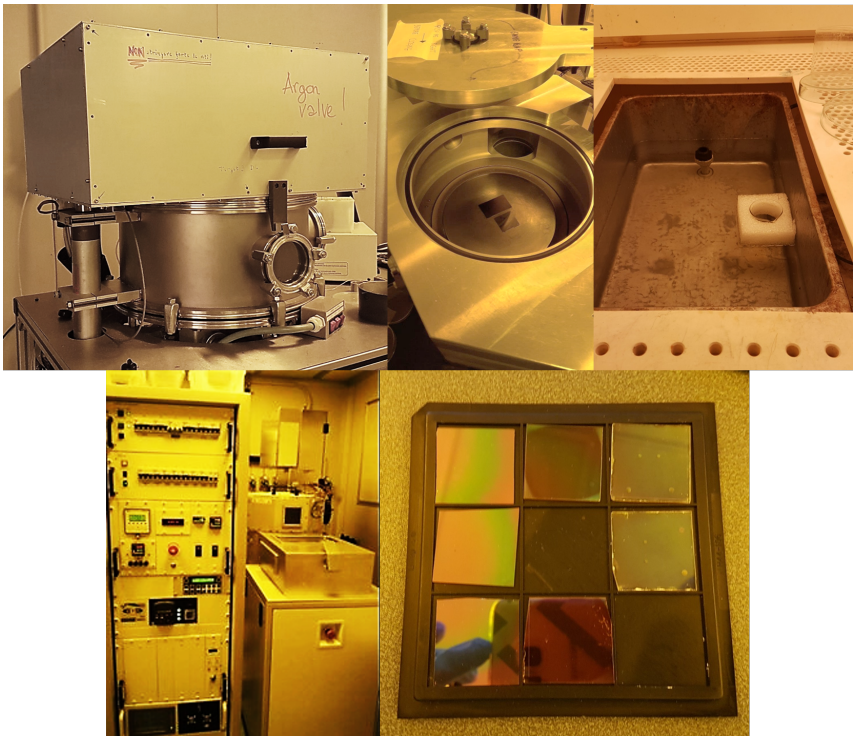

Figure 5.9: Pictures of Magnetron sputtering machine, RIE chamber, sonicated acetone soak for lift-off, ICP-RIE machine, picture of metalenses fabricated and silicon sputtered glass slides.

structures. This is done in order to proceed cautiously to verify the resistance of the hard mask during the etching process. The etching rate of the machine is estimated to be $1.6nm/s$. The etching times applied are: 4min30s, 4min50s, 5min. At first optical microscope analysis, the pattern looked well developed also with the longest process, for which the foreseen thickness is 480 nm. Successive SEM images acquisition also showed the quality of the structures and their effective height (Section 6.1).

Second fabrication procedure

A second fabrication was attempted for the metalenses replica process. This was done in order to improve the surface roughness of the metalenses samples of the first fabrication, as the morphological characterization highlights in Section 6.1. This problem was overcome by repeating the lithography process for the master production, which caused the problem. Due to the unavailability of evaporator and sputtering machine, the lens was replicated from the master by two subsequent imprinting procedures, in order to invert the pattern tone twice, i.e. return to the original tone.
The first imprinting is realized with a hydraulic Weber press on a glass substrate and

ormocer resist. The height structure for both the master and the first imprinted sample is about 250 nm. The second imprinting was done on the glass, silicon sputtered, slides, using the ormocer as a master, with a UV lithography technique, since the master for this operation is transparent to UV light. The etching process was carried out directly, since the resist used allowed a ratio between the final and starting thickness equal to 2, allowing to reach exactly the desired thickness of 500 nm. Anyway, the design was not seized for this fabrication procedure and did not account for a lateral etching of this magnitude.
This fabrication attempt was realized anyway in order to test the good quality of the substrate for the future samples, which was successful. This results are reported in Section 6.1.

Chapter 6

Characterization

The fabrication produced multiple metalenses samples, differing for the etching time (Section 5.2). In the following we will refer to the sample with etching time $t = 4$ min 30 s as "sample A" and to the sample with etching time $t = 5$ min as "sample B". The morphological characterization is entirely focused on sample A, while the optical characterization considers both the samples.

6.1 Morphological characterization

After the fabrication the metalens samples were subjected to Scanning Electron Microscope (SEM) analysis. Images were acquired both with the sample in a planar configuration, for deducing the real dimensions of the fabricated pillars and their distance, and with a tilting of 45°, in order to measure the height of the structures. The parameters deduced will be then compared with the design.

On the left of Figure 6.1 it is showed the entire patterned area. The radial lines highlighted by the image correspond to an abrupt change in the pillar orientation, and in their shape as well. A portion of one of these lines is present in the picture on the right too. This picture shows the outcome of the pattern fabrication. The pillars are clearly present and distinguishable, but they are truncated pyramids rather than prism-shaped. The height of the structures in this picture was estimated to be (440 ± 10) nm. The contributions to the estimate error are: the size of the pixel in the image, the SEM accuracy, and the uncertainty on the pillar boundaries identification. Anyway, since the analysis was performed on quite a big number of pillars, the error turned out to be almost entirely due to SEM accuracy. The height does not correspond to the designed one

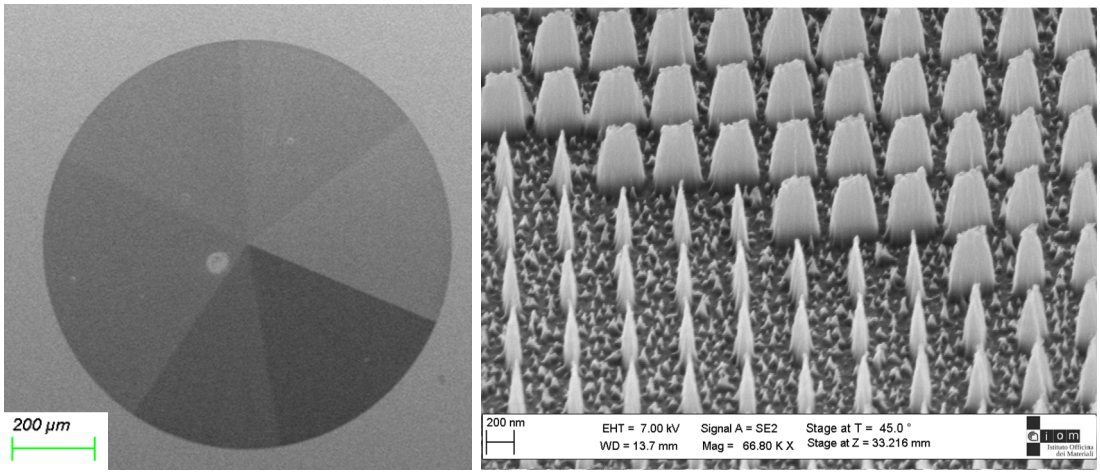

Figure 6.1: SEM images of the ML with 200 μm and 200 nm scale. The image on the right was acquired with 45° tilted sample

(500 nm), the reason is to be found partially in an insufficient etching time; the tapered profiles of the pillars, instead, suggest a degradation of the chromium mask in the final part of the etching procedure.

With the acquired data, it was possible to analyze the distance between the centres of the pillars and their base dimensions and compare the experimental and theoretical data. A picture was acquired at the exact centre of the ML, and compared to the same portion of its design, as visible in Figure 6.2. The CAD pattern is the one used for the EBL master lithography, so the pillar sides are bigger of 40 nm then the desired ones, as explained in the fabrication Chapter 5.2. At first sight the pattern well matches the design.
The picture was analyzed with ImageJ software with the 'Analyze particle' function.

Concerning the pillar dimensions, because of the tapered shape of the pillars, the dimensions we deduce from this picture correspond to the basis of the pyramid trunks.
In order to compare each pillar to its corresponding design version, also the CAD image was analyzed with ImageJ. A pillar list was created ordering them by position and paired with the list of real pillars. The CAD pillars were then sorted according to their shape by analyzing their geometry and paired with their real counterpart.
For each kind of pillar, the dimensions are reported in histograms and compared to the theoretical dimensions (red line in Figure 6.3). One pillar is represented by a column of two plots. The green columns represent elliptical pillars. The pillar dimensions are not represented by sharp functions and the designed quantities are not always included in

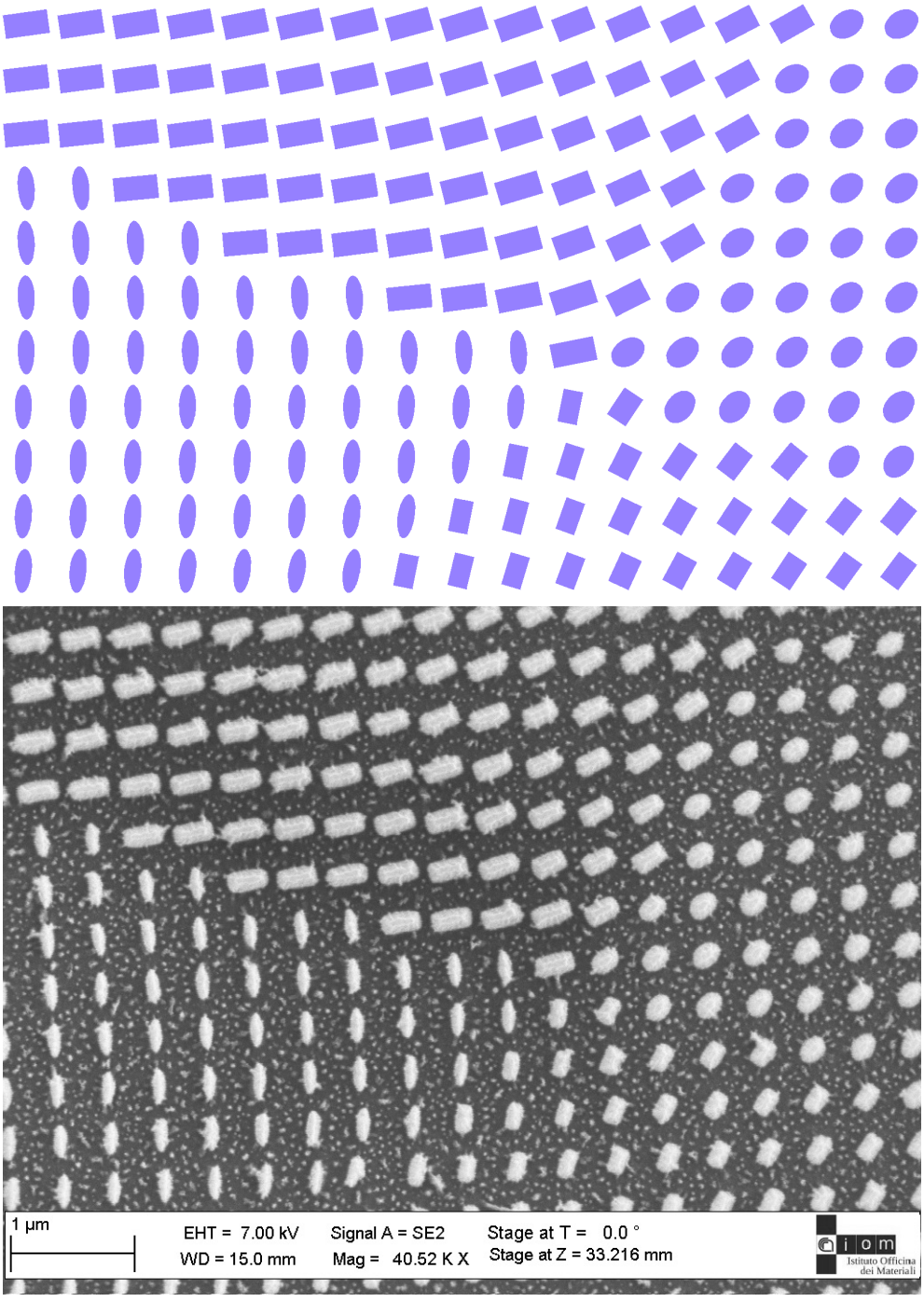

Figure 6.2: Comparison between the designed pattern (blue) and the experimental one in the centre of the ML.

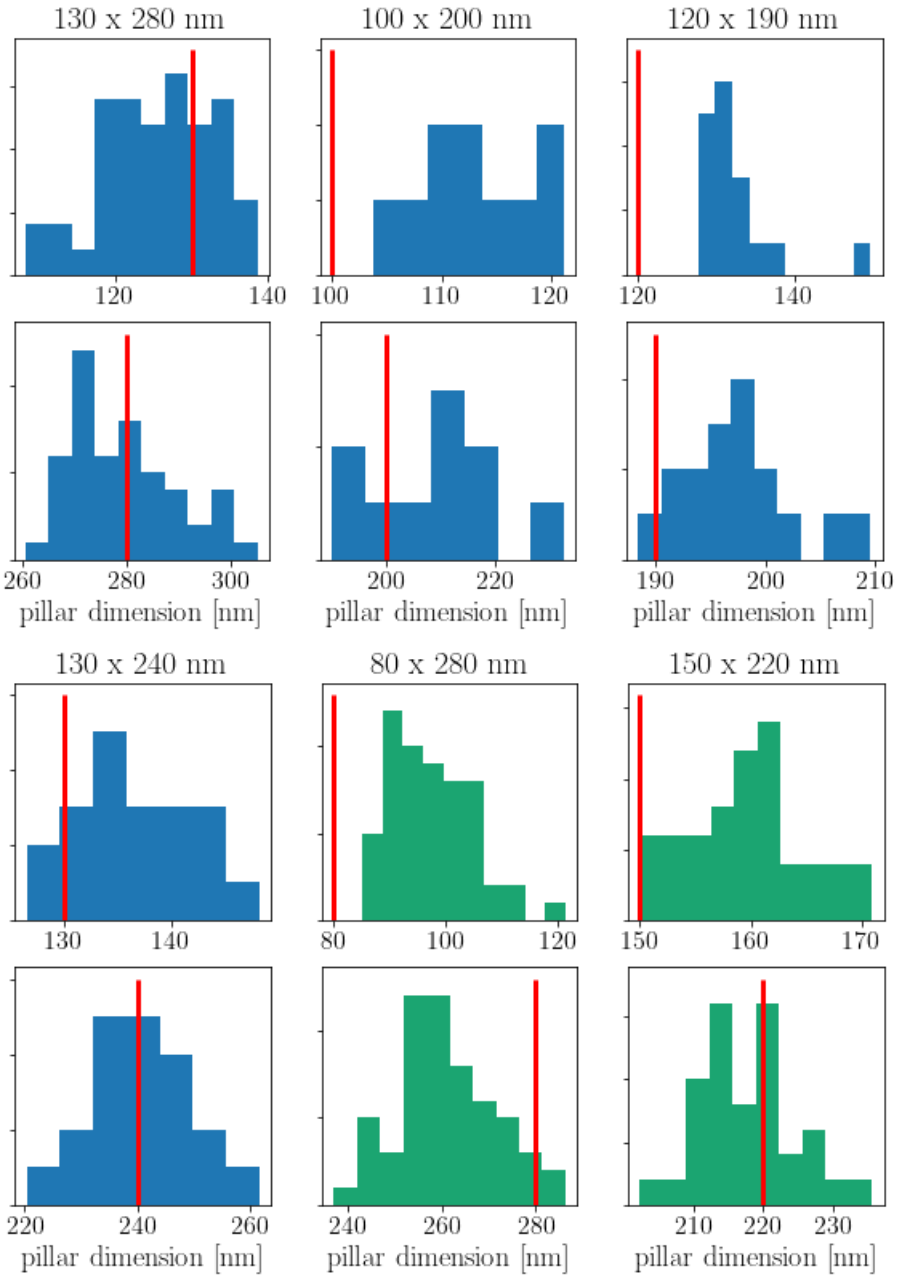

Figure 6.3: Histograms of the pillars dimensions and comparison with design dimensions (red line). The blue plots represent rectangular-based pillars. The green graphs represent elliptical pillars.

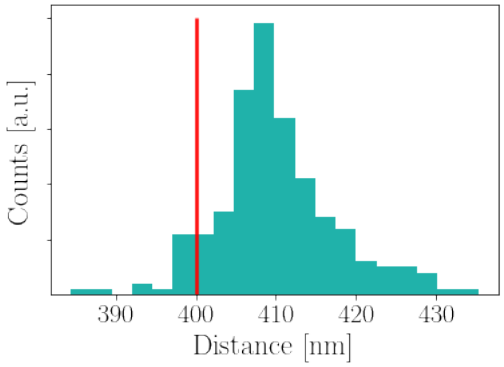

Figure 6.4: Histogram of the distances between the pillars centroids of the SEM picture in Figure 6.2. The designed distance is 400 nm.

the experimental intervals. Anyway there is agreement between design and realization.

Lastly, the distances deduced from the image in Figure 6.2 are reported in Figure 6.4. The distance value was calculated as (410 ± 10)nm. This value has a good compatibility with the designed one (400 nm). This measure is not related to etching procedure or other fabrication variables, so it was expected to be in agreement with the design.

For the morphological characterization it is important to underline another defect in fabrication: the substrate at the base of the pillars shows an evident roughness. This can be seen in bot Figure 6.1 and 6.2. This feature reflects the master quality, which suffered of the same problem. This issue was solved by repeating the lithography process for the master, bringing to the result in Figure 6.5 for the fabricated sample. The samples from the new master, i.e. without roughness, due to the fabrication techniques adopted, show a clear size-shrinkage, due to the excessive etching time, which was necessary in order to reach the desired heights.
It was taken the decision of optically characterizing the samples with roughness, and to discard the others. The irregularity in the base does not have a height comparable with the pillars'. It is expected to cause a blurring effect in the optical images, without altering significantly the metalens behaviour.
On the contrary, having pillars that don't match significantly the design means altering the optical behaviour. A next fabrication round should combine both positive aspects.

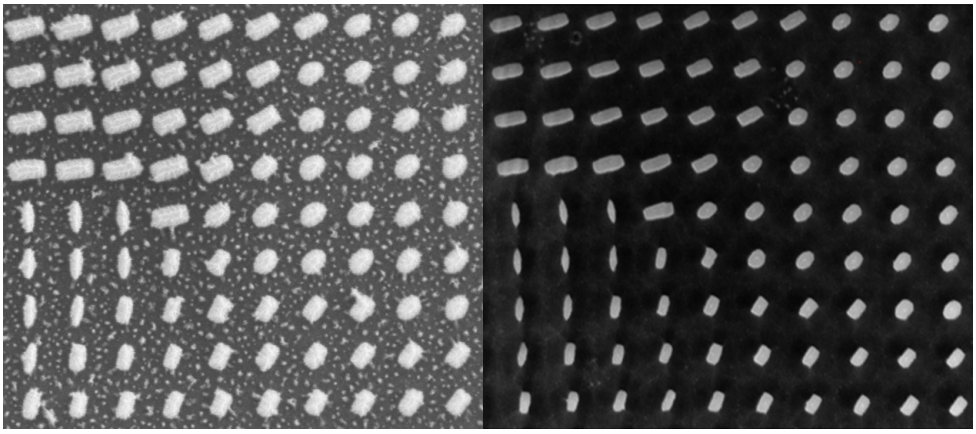

Figure 6.5: Central area of the metalens for a sample produced with the first and second master. The new sample doesn't present substrate roughness, but it suffers of pillar dimensions shrinkage.

6.2 Optical characterization

The metalenses samples were characterized via laser illumination. Here it is reported the detailed characterization of the sample A and sample B.
The characterizazion was carried out with a SuperK COMPACT supercontinuum laser, coupled with a SuperK Varia monochromator with range [450 : 850] nm. The lens was illuminated and a converging lens with focal length of 20 cm is used in an f-f configuration for paring it to the camera. A reflective filter $ND = 2.0$ is used to attenuate the intensity, for not saturating the camera.
The scheme representing the optical elements used for the characterization is shown in Figure 6.6. Since the DFML works with input circular polarization, the laser beam has to be polarized. The circular polarization can be realized by combining a linear polarizer and a quarter wave plate whose fast axis must be oriented at 45° with respect to the linear polarization direction, or −45°, according to the handedness of the desired circular polarization.

When the beam is polarized it can impinge on the ML, but in this case the beam waist was bigger than the ML diameter, so the image suffered of border effect. To overcome this issue, the beam transverse section can be reduced using two converging lenses with different focal lengths f_1 and f_2, positioned with coincident focal points. The ratio between the final and initial beam size is equal to the ratio of the focal lengths:

$$r = \frac{f_1}{f_2} = \frac{w_1}{w_2} \tag{6.1}$$

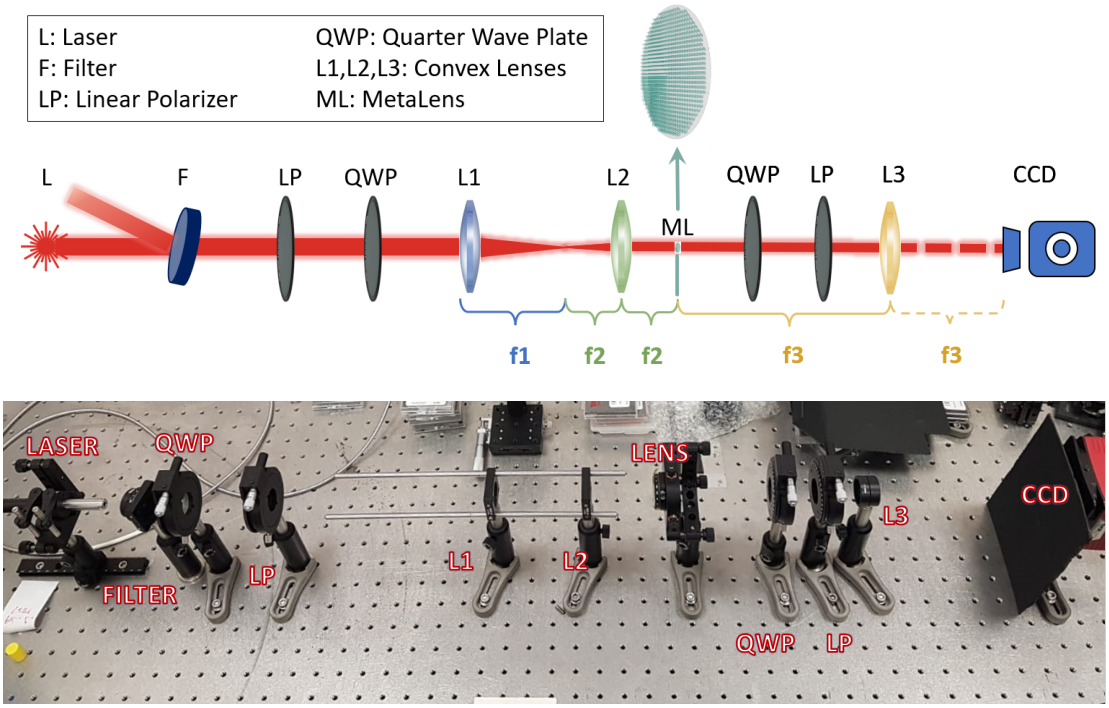

Figure 6.6: Optical line scheme for DFML characterization, and picture of real setup. The line is composed with laser, circular polarizer, lenses in 4f configuration, ML, circular polarizer, lens in f-f configuration, CCD camera.

In order to choose the right ratio, an image of the inaltered beam (without the ML and the lenses with f_1 and f_2) is taken and its size is measured by fitting the image with a two-dimensional gaussian, as reported in Figure 6.7.

The beam waist as a fit parameter deduced from this image is $w_b = 0.99 \pm 0.01$ mm, which means that the parameter of the gaussian function representing its intensity is $\sigma_b = w_b/2 = 0.495$mm. The 99% of the intensity of a two dimensional gaussian is contained in a circular support of radius $3\sigma_b$. So it is desirable to have

$$3w_b < \mathrm{d}_{ML} \tag{6.2}$$

where $\mathrm{d}_{ML} = 1$ mm is the diameter of the metalens. This means that the ratio in Equation 6.1 must be at least $r = 3$. Because of lens availability in the laboratory, it was chosen $f_1 = 100$ mm and $f_2 = 25$ mm, so that the beam reduced its size four times.

Going back to the optical line (Figure 6.6), the ML should change the spin momentum

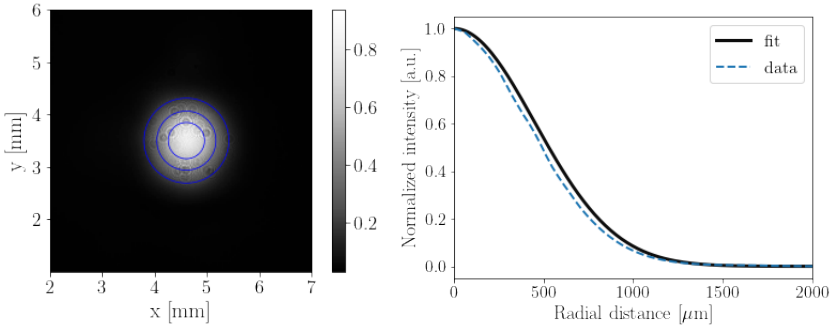

Figure 6.7: Gaussian beam at 775 nm, with 2d gaussian fit. The value for the beam waist is 990 ± 10 μm.

from $+1$ to -1 or viceversa, according to Equation 3.8. Anyway, in case of non-ideality, the zero order term of the equation may not be completely suppressed. To eliminate this hypothetical contribution, the circular polarization corresponding to the one generated before the ML is cut by orienting the second wave plate at an orientation of 90° with respect to the first one, and then applying a linear polarizer perpendicular to the first one.

Polarizers effect in Jones' formalism In the following it is reported the proof that this system filters only the zero order term. The basis of Jones' formalism is in Section 2.4.

Suppose the initial LP is vertical, and the first QWP is oriented at +45°. The order zero component maintains this polarization state after crossing the metalens, i.e. LCP, while the first order is RCP. The effect of applying a −45° QWP on the first order $\frac{1}{\sqrt{2}}[1, -i]^T$ is:

$$\frac{1}{2}\begin{bmatrix} 1 & +i \\ -i & -1 \end{bmatrix}\begin{bmatrix} 1 \\ -i \end{bmatrix} = \frac{1}{2}\begin{bmatrix} 2 \\ 0 \end{bmatrix} = \begin{bmatrix} 1 \\ 0 \end{bmatrix} \tag{6.3}$$

which is an horizontal polarization, and it is unaffected by passing through the last horizontal polarizer. The zero order $\frac{1}{\sqrt{2}}[1, i]^T$ becomes:

$$\frac{1}{2}\begin{bmatrix} 1 & +i \\ -i & -1 \end{bmatrix}\begin{bmatrix} 1 \\ i \end{bmatrix} = \frac{1}{2}\begin{bmatrix} 0 \\ 2i \end{bmatrix} \rightarrow \begin{bmatrix} 0 \\ 1 \end{bmatrix} \tag{6.4}$$

which is a vertical polarization, thus it is filtered by the last horizontal polarizer.

Eventually, the metalens is conjugated with the CCD camera with a converging lens with $f_3 = 200$ mm.

Images were acquired in a wide range of wavelengths for both the starting circular polarizations. For both samples A and B, the outcoming beam displayed the double functionality: in the OAM intensity profile the expected doughnut profile is recognizable because of the presence of a dark central region, though the images are not perfectly symmetric. Also the gaussian beam is recognizable. The intensity maps don't display a high quality shape, but the two functions are clearly recognizable and, most importantly, distinguishable. This confirms the generation of independent beams with the two desired wavefronts, with the output can be controlled by the input circular polarization handedness.
The double behaviour is not present in an evident way at the design wavelength $\lambda_d =$ 775nm, but it was observed around $\lambda_A = 695$ nm for sample A and $\lambda_B = 680$ nm for sample B. The images acquired around these wavelength for the two functions are shown in Figure 6.8.
The double functionality is visible with a better quality in the centre of the wavelength intervals showed in the picture. The doughnut is the most critical feature to detect: it results more visible for sample B and for a larger wavelength range.

Then the intensity profiles of both functions are analyzed with a customized code and compared to the expected profiles, which are respectively the gaussian reference beam, and a Laguerre gaussian beam having as beam radius the radius of the reference gaussian. The gaussian beams produced by the metalens are compared with the reference beam acquired with the setup without the metalens in Figure 6.9. Its image was fitted with a 2-D gaussian: its level curves are represented with blue ellipses. Those curves are then superimposed to the gaussian function image produced by the metalenses A and B to make a comparison (Figure 6.10 and 6.11 top-left). The radial intensity profile of the beam is then computed at the wavelengths of interest (Figure 6.10, 6.11, top-right) and the radial profile of the ideal gaussian is reported in black. The radial intensity profile is computed by integrating the intensity inside shells of variable distance from the centre. The profile of the OAM beam was analyzed with a custom made algorithm that recognizes its centre because of its low intensity, which is at the same time surrounded by high intensity pixels. Starting from the centre, the radial intensity profile is computed (Figure 6.10, 6.11, middle-right). In this case its values approximate zero at the origin, then grow in correspondence of the doughnut ring, then decrease again. In this plot it is also reported the ideal intensity profile of a Laguerre-Gaussian beam,

$$I(\rho) = \frac{2\rho^2}{w_{\text{ref}}^2} e^{-\frac{2\rho^2}{w_{\text{ref}}^2}} \tag{6.5}$$

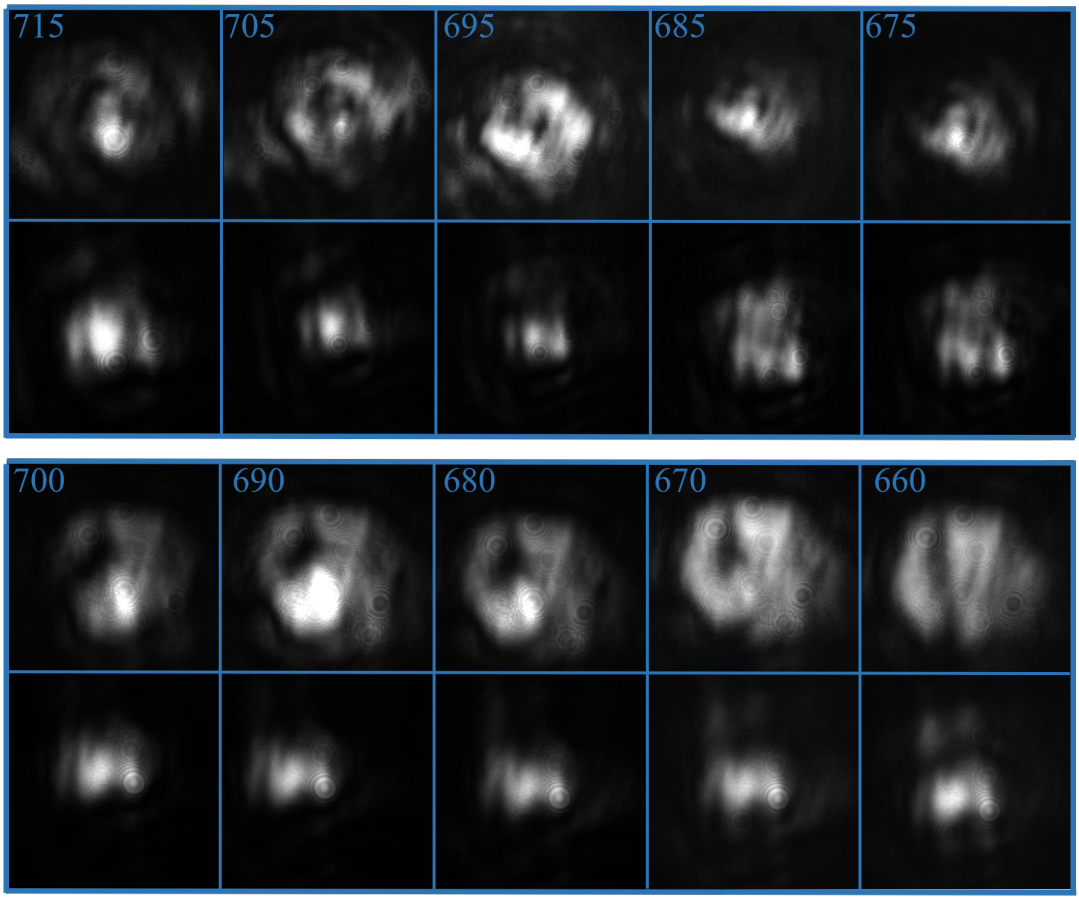

Figure 6.8: Optical images for sample A, on top, and sample B, in the bottom. The double functionality is shown for the wavelength range with the best behaviour. The wavelength for each colums of pictures is in nanometer unit.

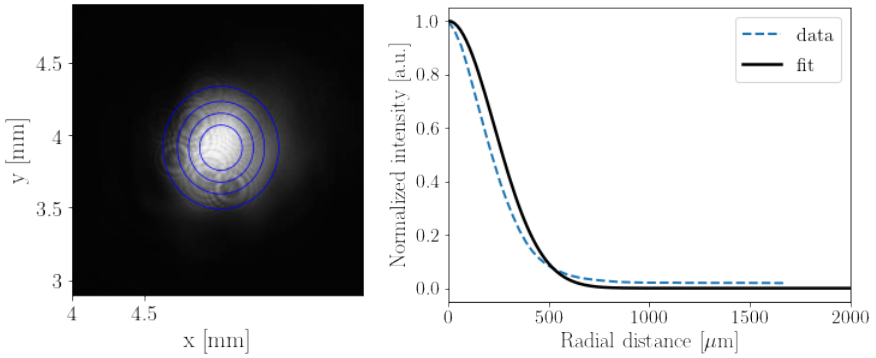

Figure 6.9: Reference gaussian beam fitted for comparing it with the gaussian and OAM function intensities.

considering as beam radius w_{ref}, which was previously computed from the fit of the gaussian beam with empty setup. The experimental and computed curves are in agreement for sample B, except for the portion at larger radial distance, where there is some displacement due to the intensity broadening of the OAM in the top right area of the image. For sample A the profile with smaller wavelength shows a huge displacement from the reference, but the other curves quite match the prediction.
The red axes plotted over the doughnuts were considered for computing the intensity profile over them. They are reported in the Figure 6.10, 6.11, bottom-left and display two peaks with a minimum between them, even though these functions are not completely symmetric. On the right of this plot it is reported a table with the Michelson contrast of the doughnuts. The contrast definition is:

$$C_M = \frac{I_{max} - I_{min}}{I_{max} + I_{min}} \tag{6.6}$$

where I_{max} is the maximum between the intensities integrated along the shells of constant radius, and I_{min} is the minimum intensity in the dark region inside the doughnut.
Its values are significantly greater than zero, with very good values for the central λ, for both the samples.

The result showed the correct functioning of the fabricated lenses. The wavelength-band with optimal functioning has revealed to be very short: [670 : 690] nm for sample A and [695 : 705] nm for sample B, though a correct behaviour of poorer quality is clearly visible in the wavelength interval [640 : 700] nm for sample B. Besides, it was observed the correct circular polarization handedness conversion for a wide wavelength range. During the characterization process, the lenses were mounted on a moving stage at it was clearly visible that the transmitted intensity reached a maximum when the lens intercepted the otical axis.

Probably, the lack of accuracy in the structure fabrication, as analyzed in section 6.1, did not compromise the lens behaviour, but only the conditions at which it is carried out. As a first fabrication process, the results are promising, especially because the intensity profiles related to the two functions are clearly distinguishable, the radial profiles agree with the predictions and the contrast values are noteworthy. There is potential for improvement, as will be mentioned in section 8.

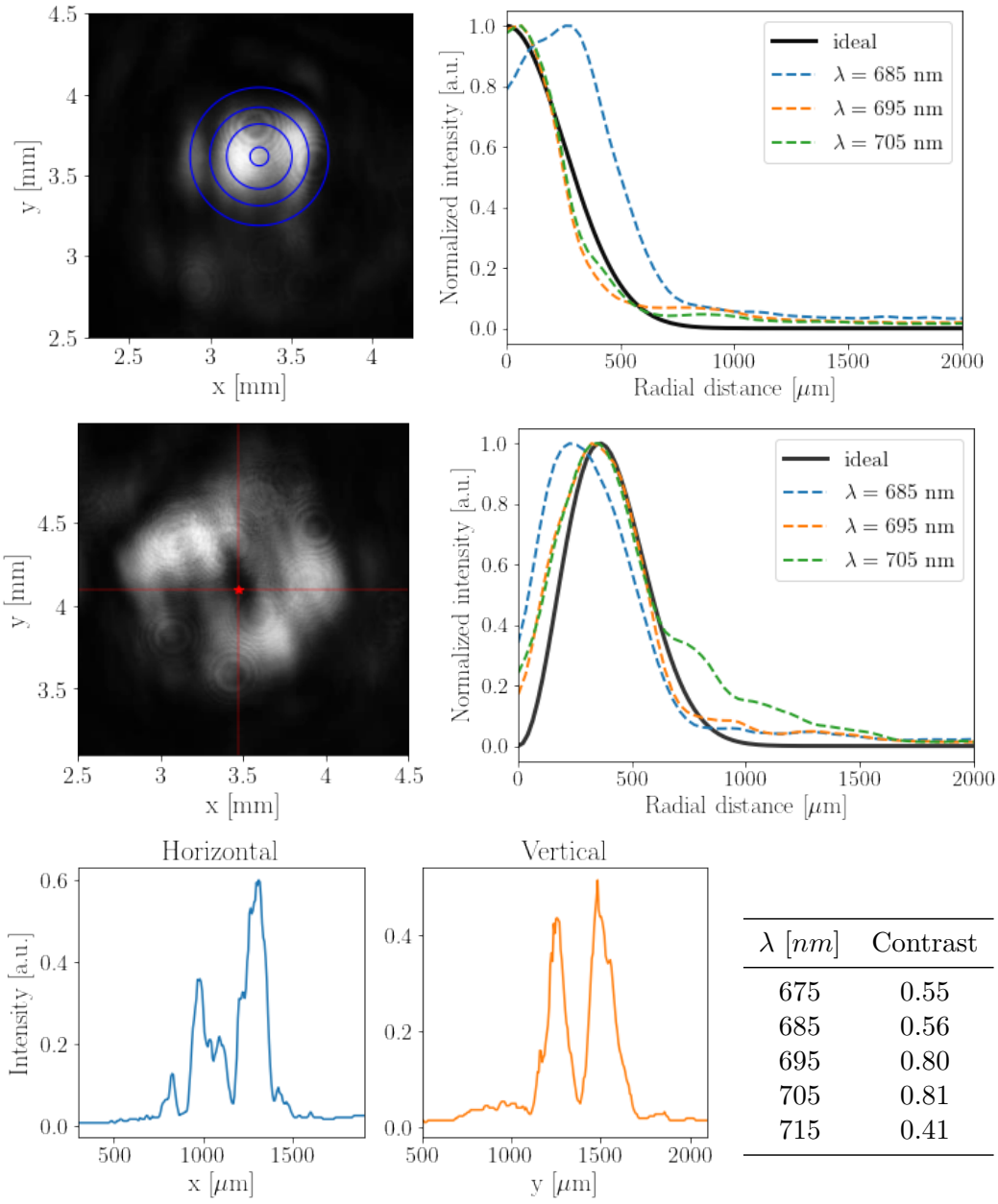

λ [nm]	Contrast
675	0.55
685	0.56
695	0.80
705	0.81
715	0.41

Figure 6.10: Top,left: gaussian beam function image at $\lambda = 695$ nm with fitted 2-D gaussian in red. Top,right: radial intensity profiles with the fit for $\lambda = 695$ nm. Middle,left: OAM beam function image with centre and axes passing for the centre (red). Middle,right: radial intensity profile with theorical Laguerre-Gauss distribution. Bottom, left: intensity profiles over the axes intersecting the center of the OAM image. Bottom, right: Michelson contrast of the doughnuts

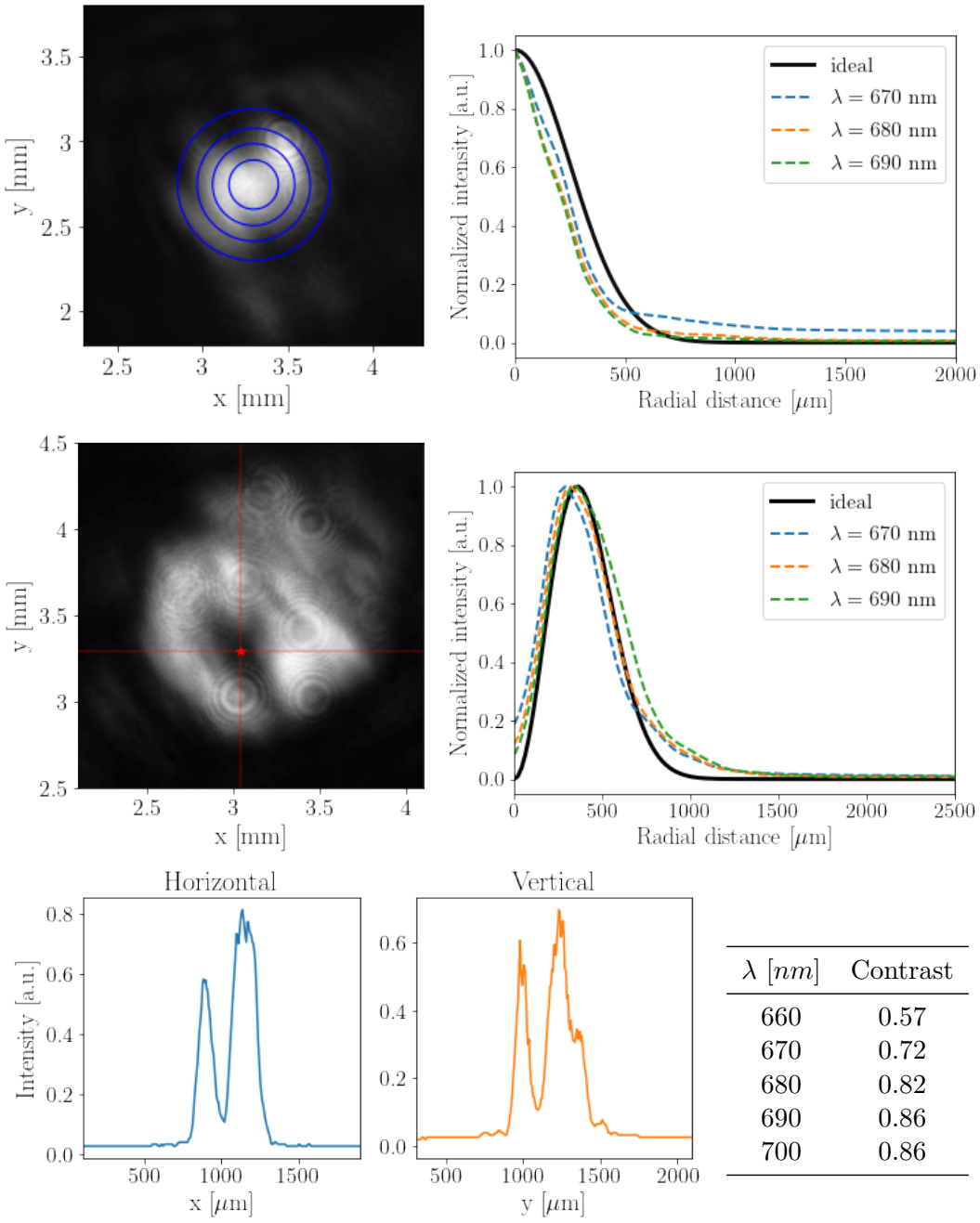

λ [nm]	Contrast
660	0.57
670	0.72
680	0.82
690	0.86
700	0.86

Figure 6.11: Top,left: gaussian beam function image at $\lambda = 680$ nm with fitted 2-D gaussian in red. Top,right: radial intensity profiles with the fit for $\lambda = 680$ nm. Middle,left: OAM beam function image with centre and axes passing for the centre (red). Middle,right: radial intensity profile with theorical Laguerre-Gauss distribution. Bottom, left: intensity profiles over the axes intersecting the center of the OAM image. Bottom, right: Michelson contrast of the doughnuts

Chapter 7

Characterization comparison

In this section a commercial SPP device and a nanofabricated q-plate will be optically inspected in order to compare the results with the OAM produced by the bi-functional metalenses object of this work. The basic principles of functioning of these devices are reported in Section 3.1 and 3.3.

7.1 SPP

The SPP device was characterized before the dual-function characterization in order to get acquainted with the OAM-carrying beams characterization methods, since the optical line is more basic. The optical line contains the same fundamental elements of

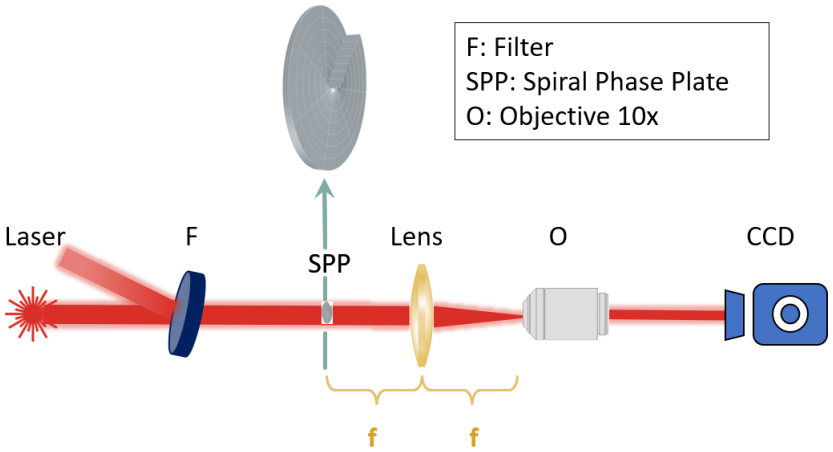

Figure 7.1: Optical line for SPP characterization

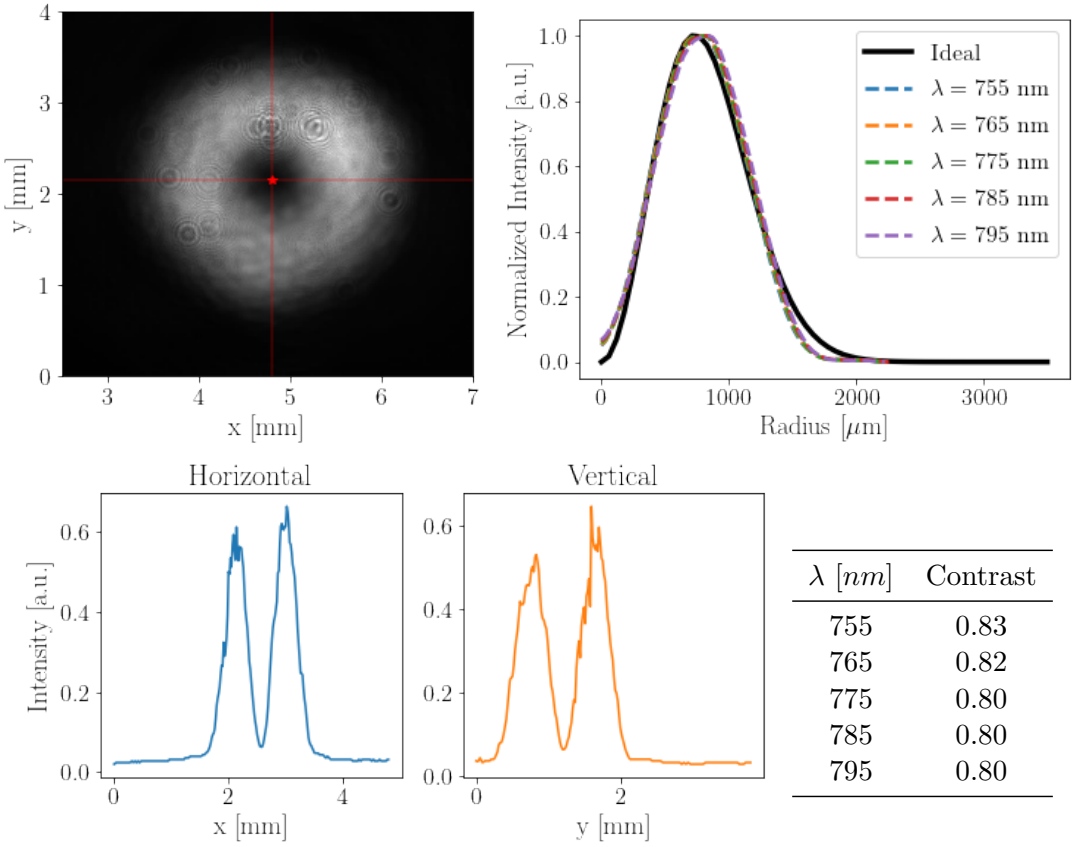

λ [nm]	Contrast
755	0.83
765	0.82
775	0.80
785	0.80
795	0.80

Figure 7.2: CCD camera picture at 775 nm wavelength with the doughnut, its centre and horizontal and vertical axes (left). Intensity profiles along the radial direction (right)

the line used for the metalens characterization, with the absence of polarizers, since the SPP can work with both polarized and unpolarized beams. The beam size was already the right dimension in order to highlight the OAM generation effect illuminating most of the lens without incurring in border effects. The f-f system conjugates the SPP to an objective, a 10x magnifier, which is infinity conjugated with a CCD camera. This element was introduce in order to magnify the image spot. The scheme is reported in Figure 7.1.

The image was acquired for five wavelengths around the design $\lambda = 775$ nm with a step of 10 nm between them. Then the radial intensity profile and the Michelson contrast were computed (Figure 7.2, left).

The data for the characterization of the SPP shows a very good quality doughnut for the whole wavelength interval considered in the graphic, but its optimal functioning rnge was estimated to be very large: [650:850] nm.

7.2 Q-plate

Another metalens, previously fabricated by Prof. Romanato's group, with a similiar recipy with respect to the DFML was fabricated. The aim is to compare the OAM quality of a different device, but fabricated with the same techniques. The optical line is the same used for the DFML characterization, with a difference in the 4f system. Since the q-plate diameter is bigger (1.2 mm), the beam size reduction applied was of 2.5 times, through lenses with focal lengths of $f_1 = 125$ mm and $f_2 = 50$ mm. The characterization steps are the same used for the previous procedures.

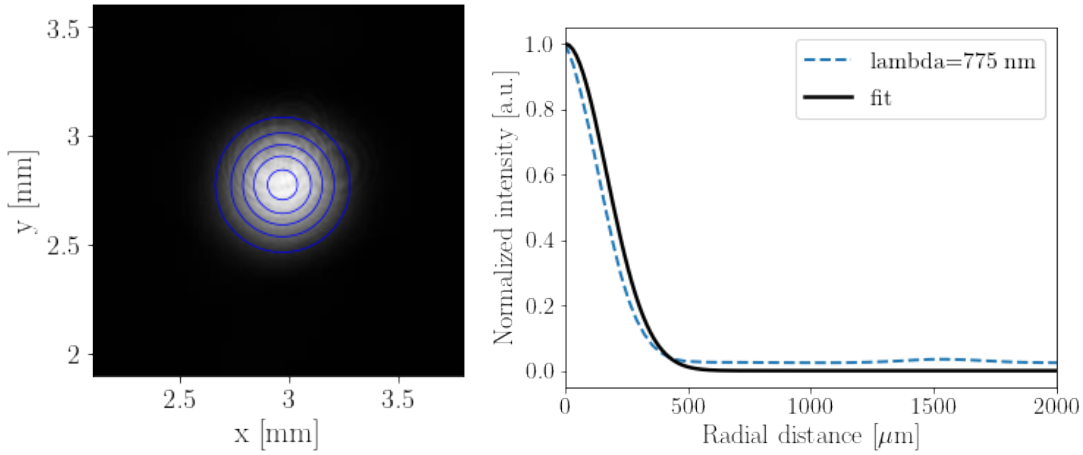

Figure 7.3: Gaussian beam two dimensional fit and its representation as radial profile. The beam fitted waist size is $w = 340 \pm 10$ μm.

7.3 Comparison

Regarding the intensity uniformity and the overall impression over the OAM quality, the SPP turned out to have better performances. Anyway, the results obtained with the the metalenses have a discrete quality, considering that the fabrication had been realized for the first time. The comparison with the real and ideal radial profile showed good agreement in all the cases, also for the bi-functional lenses. Also the contrast showed a similar performance for all the metalenses, with the SPP displaying more stable values, while for the metalenses its value is more sensitive to the wavelength, but is, in some cases, closer to 1 than the SPP contrast. Regarding the q-plate, it generates a good-quality doughnut, which confirms that the fabrication techniques, which are the same adopted for the dual function MLs, can bring to good results at the end of an

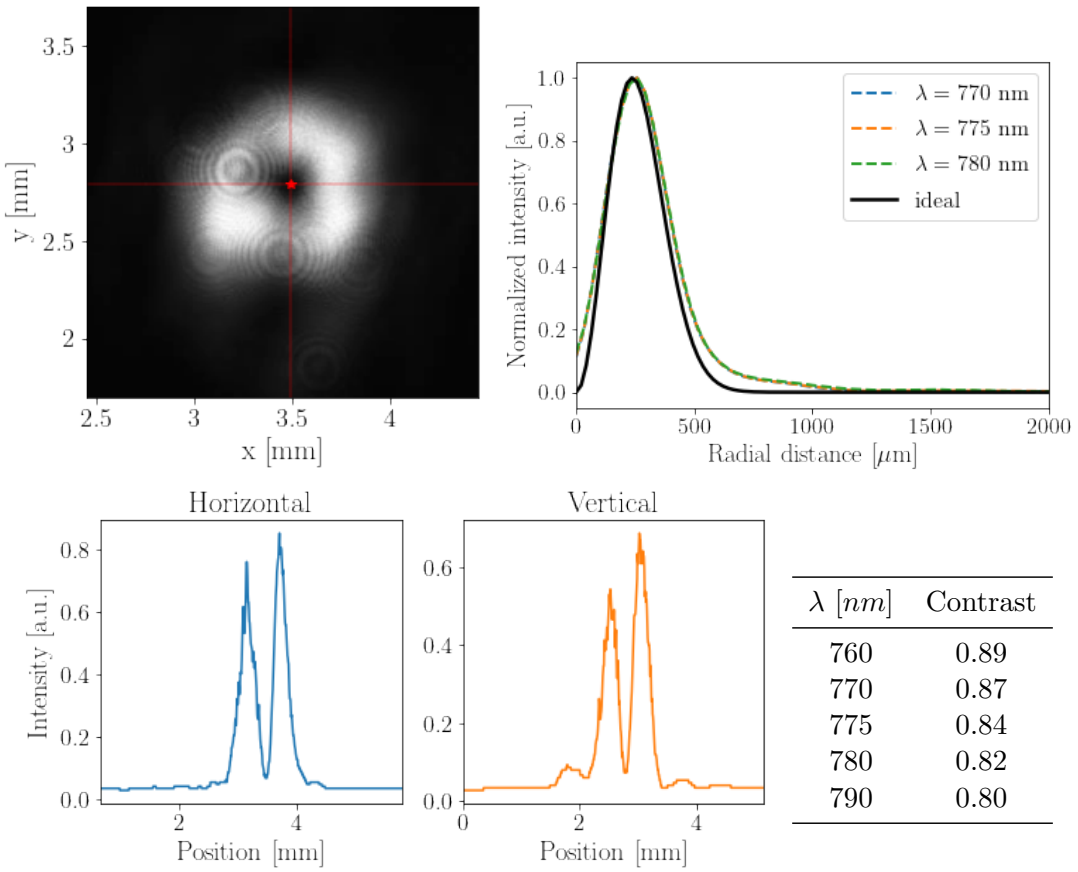

λ [nm]	Contrast
760	0.89
770	0.87
775	0.84
780	0.82
790	0.80

Figure 7.4: CCD camera picture at 775 nm wavelength with the doughnut, its centre and horizontal and vertical axes (left). Intensity profiles along the radial direction (right).

optimization of the fabrication procedure.
To sum up, the best optical results produced up to now in term of doughnut quality are related to the SPP and the q-plate. Anyway the dual function metalenses are a project still in developement and the strategies for improving the samples quality have already been identified (Section 8). It is noticeable in particular that the metalenses object of this work have the more advanced feature of managing two independent wavefronts by controlling the input polarization.

Chapter 8

Future perspective

Fabrication tuning

The fabrication should be improved to avoid the pillars tapered profile, thus to adjust their height and the adherence of the in plane dimensions of the pillars with the designed ones. The first problem can be solved by using an evaporator for the hard mask deposition, rather than the sputtering, and deposite a higher thickness, in order to prevent its complete degradation before the substrate etching process is concluded. The height can be improved by a better calibration of the etching rate, by comparing the etching time to the measured heights of the structure imaged with SEM. The second problem is partially due to non-uniform lateral etching, and due to the choice of the overestimation of the pillar sizes for the master lithography. Since this problem requires a calibration process, an array with multiple equivalent metalenses can be designed and fabricated. Each metalens should have a different overestimation of the dimensions. This overestimation can be based on the previous fabrication outcome and be targetted in order to compensate the differences also with a non uniform overestimation, depending on the pillar shape. This array can be produces in different replicas, each one with a different etching time, in order to reach the desired height.

Characterization features

In order to investigate the OAM phase profile it is possible to create an interference between the structured beam and a gaussian beam. In this case there is the generation of an interference pattern according to the angle of incidence between the beams. As shown in Figure 8.1, the interference with a collinear gaussian beam with the same

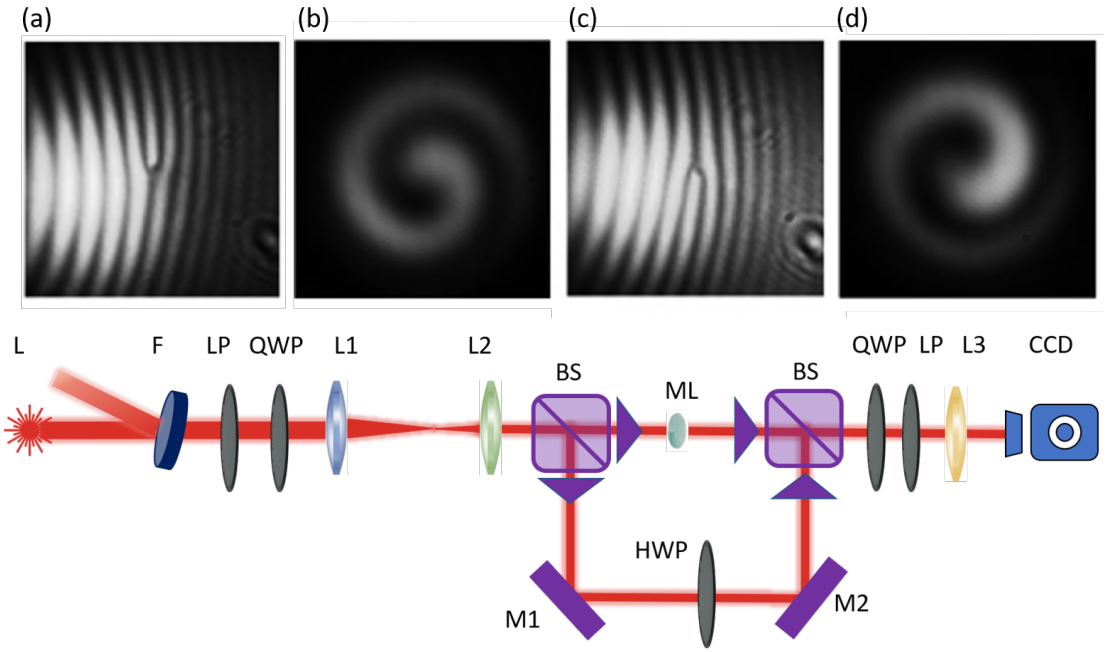

Figure 8.1: a-b) Interference pattern of an OAM beam with l=+1: collinear (a) and non-collinear (b). c-d) Same patterns with l=-1 [42]. The scheme below is the optical line necessary for realizing the interference

polarization gives a spiral interferogram if the beams are collinear, a so called fork-hologram it those incide with an angle different from zero. Figure 8.1-a,b and 8.1-c,d differ in the sign of the OAM charge $l = \pm 1$. In the bottom of figure 8.1 it is showed the optical line for the generation of the interference. The beams must interfere with the same polarization in order to maximize the intensity modulation (thus the contrast) in the interference pattern. [41] To do so, the reference gaussian beam is obtained from the CP beam with a beam splitter, and passes through a half-wave plate, to acquire the same polarization given by the metalens. Another beam splitter takes it back to the pricipal line, where it passes through the QWP an LP that filter the zero-th order polarization of the metalens. The beams are focused by an f-f lens.

Double focal metalens

Another possibility concerns the relization of a metalens which focalizes the image at f_1 with LCP and at f_2 with RCP.

The illumination simulation was performed considering a lens designed for realizing a focus at $f_1 = 1$ mm and $f_2 = 2$ mm. Also in this case we can appreciate the double

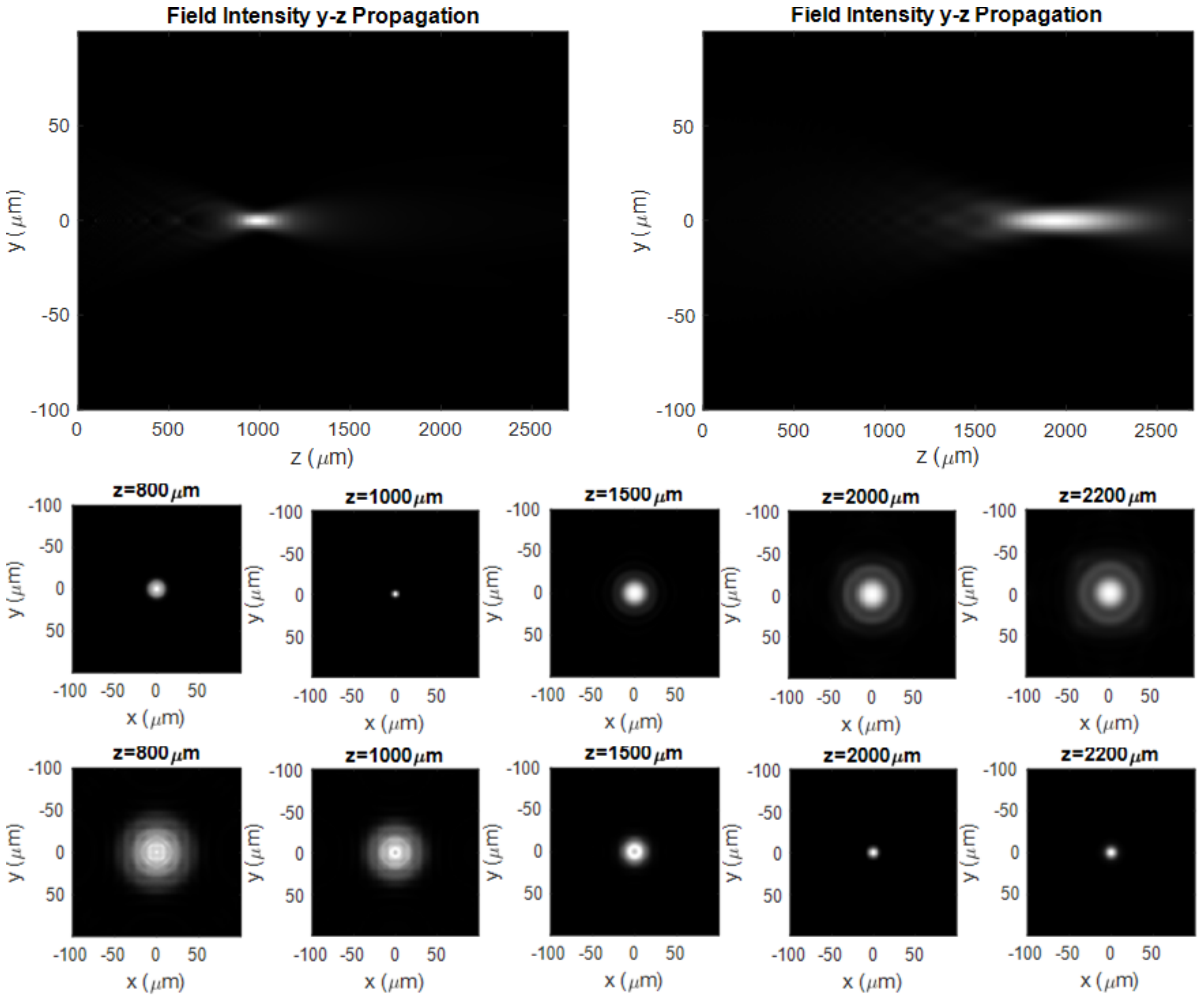

Figure 8.2: Simulation of dual focus metalens. The simulation is carried out with the simulated phase discretization.

functionality. From the x-y plots it is possible to see the beam waist decreasing in correspondence of the desired focal length (Figure 8.2). This additional simulation gives a further confirmation of the correct functioning of the metalenses phase transmission design, and allows to test their flexibility in realizing a variety of phase profiles.

Contrast phase microscopy

The contrast phase imaging is based on isotropic edge detection of a sample. The selection of fast-varying frequency components in the image spatial domain is realized by Fourier transforming the image and utilizing the lens as a filter for the low-frequency

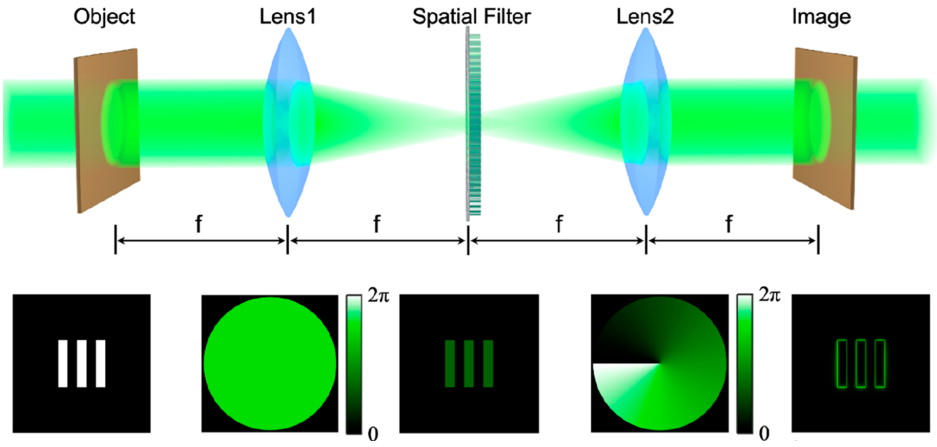

Figure 8.3: Optical line for image filtering and schematized result [24].

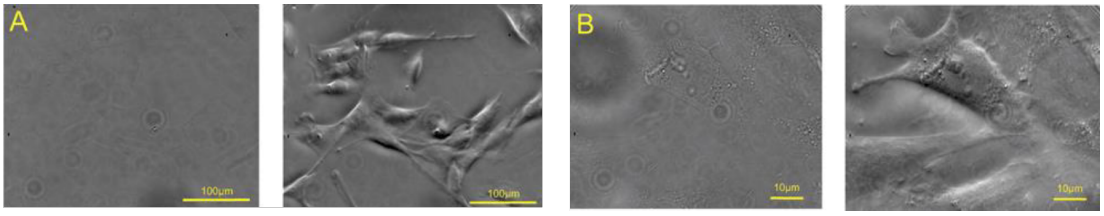

Figure 8.4: Microscope images of fibroblast cells. Each couple of images represents the same object: the images on the left show the bright-field images, whereas at the right are the corresponding spiral phase-filtered images [43].

components in the Fourier domain. The image is then anti-Fourier transformed by another focusing lens (Figure 8.3). [24] In other words it is possible to achieve two-dimensional spatial differentiation operation to enhance the borders of the image. Our metalens would be able to realize both classical bright field and contrast imaging, which are two most representative operation modes in an optical imaging system, and can extract different morphological information on an object. Developing a miniature and low-cost system capable of switching between these two imaging modes is thus very attractive for a number of applications, such as biomedical imaging [24]. In Figure 8.4 it is also possible to see an example of information extracted by contrast phase imaging on a biological tissue whose features can not be described by bright field imaging.

Chapter 9

Conclusions

This thesis work described the successful realization of dual-function metalenses devices for the generation of both an OAM endowed beam and a gaussian beam, according to the handedness of the input circular polarization.

The theoretical aspects concerning metalenses were discussed, considering their functioning principles and giving examples of other devices for the OAM generation. A preliminary insight of the main theoretical topics behind beam optics and orbital momentum generation and control is provided.

In the central part of the thesis, the design process implemented for the dual function metalens project is discussed, starting form their fundamental units simulation with COMSOL, ending up with the optical layout of the simulated beams and their local phase-amplitude transmission properties. The lens behaviour was simulated with transfer function and impulse-response function methods with a home made MATLAB code. The simulation showed the correct behaviour for the device in both circular polarizations, i.e. the generation of a gaussian beam and of an OAM featured beam respectively. The project method was further analyzed by reproducing single function metalenses design for testing the correct generation of OAM beams with different values of topological charge. All the simulated intensity profiles and phase maps were compatible with the expected results.

The fabrication process, carried out at CNR-IOM nanofabrication facility, was described, indicating the first attempts of fabrication tuning and the encountered issues. Eventually, the overall process gave good results, and the device was fabricated successfully.

The real testing of the lens behaviour was done through its characterization, by means of SEM imaging at first. This morphological analysis allowed to compare the real fabricated pattern with the designed version. Although the pattern is clearly present and recognizable, the fabrication outcome was not perfect regarding pillars shape. An analysis was performed on the single meta-units for a limited portion of the surface for comparing the pillar features; this showed a broadening of the geometric dimensions and in some cases a slight deviation from the designed quantities. Anyway, a quite good adherence with the design is reported.
The most crucial verification was realized with the optical characterization. This procedure showed the correct presence of the efficiency conversion for a broad-band wavelength. The double functionality observed was noteworthy and the presence of a partially good quality doughnut intensity profile was detected, although the functioning wavelength does not match the desired one.

The orbital angular momentum generation was compared with the ones of an industrial SPP device, and of a previously nano-fabricated q-plate device. Those lenses showed a better shape feature, though the radial intensity profiles and the contrast values are similar.

Lastly, the future perspective for the improvement and applications of this metalens device are presented: a plan for the structure improvement is explained through a better pairing of design and fabrication, and a tuning of the fabrication parameters themselves. A further characterization method is also presented. The double functionality is shown to have been also applied to the design of a double focal metalens.
From the applications side, the most important for this device is the contrast phase microscopy, realizable via OAM-beam Fourier filtering. In particular this device would allow a fast switching between a classical bright field to a contrast phase imaging.

Bibliography

[1] "Wave Optics". In: *Fundamentals of Photonics*. John Wiley and Sons, Ltd, 1991. Chap. 2, pp. 41–79. ISBN: 9780471213741. DOI: https://doi.org/10.1002/0471213748.ch2. URL: https://onlinelibrary.wiley.com/doi/abs/10.1002/0471213748.ch2.

[2] "Beam Optics". In: *Fundamentals of Photonics*. John Wiley and Sons, Ltd, 1991. Chap. 3, pp. 80–107. ISBN: 9780471213741. DOI: https://doi.org/10.1002/0471213748.ch3. URL: https://onlinelibrary.wiley.com/doi/abs/10.1002/0471213748.ch3.

[3] Matthew Leigh. "High power pulsed fiber laser sources and their use in terahertz generation". In: (Jan. 2008).

[4] Stephen M. Barnett, Mohamed Babiker, and Miles J. Padgett. "Optical orbital angular momentum". In: *Philosophical Transactions of the Royal Society A: Mathematical, Physical and Engineering Sciences* 375.2087 (2017), p. 20150444. DOI: 10.1098/rsta.2015.0444. eprint: https://royalsocietypublishing.org/doi/pdf/10.1098/rsta.2015.0444. URL: https://royalsocietypublishing.org/doi/abs/10.1098/rsta.2015.0444.

[5] Wikipedia. *Fascio gaussiano — Wikipedia, L'enciclopedia libera*. 2020. URL: http://it.wikipedia.org/w/index.php?title=Fascio_gaussiano&oldid=115427479.

[6] V. Bazhenov, Mikhail Vasnetsov, and Marat Soskin. "Laser beams with screw dislocations in their wavefronts". In: *JETP. Lett* 52 (Jan. 1990), pp. 429–431.

[7] Les Allen et al. "Orbital angular momentum of light and transformation of Laguerre Gaussian Laser modes". In: *Physical review. A* 45 (July 1992), pp. 8185–8189. DOI: 10.1103/PhysRevA.45.8185.

[8] M. Massari et al. "Fabrication and characterization of high-quality spiral phase plates for optical applications". In: *Appl. Opt.* 54.13 (May 2015), pp. 4077–4083.

DOI: 10.1364/AO.54.004077. URL: http://opg.optica.org/ao/abstract.cfm?URI=ao-54-13-4077.

[9] Giuseppe Vicidomini, Paolo Bianchini, and Alberto Diaspro. "STED super-resolved microscopy". In: *Nature Methods* 15 (Jan. 2018). DOI: 10.1038/nmeth.4593.

[10] RP photonics encyclopedia. *Polarizers*. URL: https://www.rp-photonics.com/polarizers.html.

[11] Labster. *Malus's law*. 2021. URL: https://theory.labster.com/malus-law/.

[12] Wikipedia contributors. *Waveplate — Wikipedia, The Free Encyclopedia*. 2022. URL: https://en.wikipedia.org/w/index.php,%20title=Waveplate&oldid=1068453091.

[13] Nina Hong and James Hilfiker. "Mueller matrix ellipsometry study of a circular polarizing filter". In: *Journal of Vacuum Science and Technology B* 38 (Jan. 2020), p. 014012. DOI: 10.1116/1.5129691.

[14] Svetlana Khonina et al. "The Phase Rotor Filter". In: *Journal of Modern Optics - J MOD OPTIC* 39 (May 1992), pp. 1147–1154. DOI: 10.1080/09500349214551151.

[15] Masaya Uchida and Akira Tonomura. "Generation of electron beams carrying orbital angular momentum". In: *Nature* 464 (Apr. 2010), pp. 737–9. DOI: 10.1038/nature08904.

[16] Mu Ku Chen et al. "Principles, Functions, and Applications of Optical Meta-Lens". In: *Advanced Optical Materials* 9.4 (2021), p. 2001414. DOI: https://doi.org/10.1002/adom.202001414. eprint: https://onlinelibrary.wiley.com/doi/pdf/10.1002/adom.202001414. URL: https://onlinelibrary.wiley.com/doi/abs/10.1002/adom.202001414.

[17] Wei Ting Chen et al. "A broadband achromatic metalens for focusing and imaging in the visible". In: *Nature Nanotechnology* 13 (Mar. 2018). DOI: 10.1038/s41565-017-0034-6.

[18] Raghu Dharmavarapu et al. "MetaOptics: opensource software for designing metasurface optical element GDSII layouts". In: *Opt. Express* 28.3 (Feb. 2020), pp. 3505–3516. DOI: 10.1364/OE.384057. URL: http://opg.optica.org/oe/abstract.cfm?URI=oe-28-3-3505.

[19] Vadim A. Markel. "Introduction to the Maxwell Garnett approximation: tutorial". In: *J. Opt. Soc. Am. A* 33.7 (July 2016), pp. 1244–1256. DOI: 10.1364/JOSAA.33.001244. URL: http://opg.optica.org/josaa/abstract.cfm?URI=josaa-33-7-1244.

[20] Mathieu Gonidec. "Concept of non-periodic metasurfaces based on positional gradients applied to IR-flat lenses". In: *Opt. Mater. Express* 7.7 (July 2017), pp. 2346–

2351. DOI: 10.1364/OME.7.002346. URL: http://opg.optica.org/ome/abstract.cfm?URI=ome-7-7-2346.

[21] Mohammadreza Khorasaninejad et al. "Metalenses at visible wavelengths: Diffraction-limited focusing and subwavelength resolution imaging". In: *Science* 352.6290 (2016), pp. 1190–1194. DOI: 10.1126/science.aaf6644. eprint: https://www.science.org/doi/pdf/10.1126/science.aaf6644. URL: https://www.science.org/doi/abs/10.1126/science.aaf6644.

[22] Pietro Capaldo et al. "Nano-fabrication and characterization of silicon meta-surfaces provided with Pancharatnam-Berry effect". In: *Opt. Mater. Express* 9.3 (Mar. 2019), pp. 1015–1032. DOI: 10.1364/OME.9.001015. URL: http://www.osapublishing.org/ome/abstract.cfm?URI=ome-9-3-1015.

[23] Kuang Zhang et al. "High-Efficiency Metalenses with Switchable Functionalities in Microwave Region". In: *ACS Applied Materials & Interfaces* 11.31 (2019). PMID: 31296005, pp. 28423–28430. DOI: 10.1021/acsami.9b07102. eprint: https://doi.org/10.1021/acsami.9b07102. URL: https://doi.org/10.1021/acsami.9b07102.

[24] Pengcheng Huo et al. "Photonic Spin-Multiplexing Metasurface for Switchable Spiral Phase Contrast Imaging". In: *Nano Letters* 20.4 (2020). PMID: 32155076, pp. 2791–2798. DOI: 10.1021/acs.nanolett.0c00471. URL: https://doi.org/10.1021/acs.nanolett.0c00471.

[25] Yinghui Guo et al. "Spin-decoupled metasurface for simultaneous detection of spin and orbital angular momenta via momentum transformation". In: *Light: Science & Applications* 10 (Dec. 2021). DOI: 10.1038/s41377-021-00497-7.

[26] Jian Wang and Alan E. Willner. "Twisted Communications using Orbital Angular Momentum (Tutorial Talk)". In: *Optical Fiber Communication Conference*. Optica Publishing Group, 2016. DOI: 10.1364/OFC.2016.Th1H.5. URL: http://opg.optica.org/abstract.cfm?URI=OFC-2016-Th1H.5.

[27] COMSOL Multiphysics. "Introduction to COMSOL multiphysics®". In: *COMSOL Multiphysics, Burlington, MA, accessed Feb* 9 (1998), p. 2018.

[28] Christopher Hakoda et al. "Using Floquet periodicity to easily calculate dispersion curves and wave structures of homogeneous waveguides". In: *AIP Conference Proceedings* 1949.1 (2018), p. 020016. DOI: 10.1063/1.5031513. eprint: https://aip.scitation.org/doi/pdf/10.1063/1.5031513. URL: https://aip.scitation.org/doi/abs/10.1063/1.5031513.

[29] Jian-Ming Jin. *The finite element method in electromagnetics*. John Wiley & Sons, 2015.

[30] Wenhui Zhang et al. "Analysis of numerical diffraction calculation methods: from the perspective of phase space optics and the sampling theorem". In: *Journal of the Optical Society of America A* (Oct. 2020). DOI: 10.1364/JOSAA.401908.

[31] Stephen Y. Chou, Peter R. Krauss, and Preston J. Renstrom. "Imprint Lithography with 25-Nanometer Resolution". In: *Science* 272.5258 (1996), pp. 85–87. DOI: 10.1126/science.272.5258.85. eprint: https://www.science.org/doi/pdf/10.1126/science.272.5258.85. URL: https://www.science.org/doi/abs/10.1126/science.272.5258.85.

[32] L. J. Guo. "Nanoimprint Lithography: Methods and Material Requirements". In: *Advanced Materials* 19.4 (), pp. 495–513. DOI: https://doi.org/10.1002/adma.200600882. eprint: https://onlinelibrary.wiley.com/doi/pdf/10.1002/adma.200600882. URL: https://onlinelibrary.wiley.com/doi/abs/10.1002/adma.200600882.

[33] Hongbo Lan and Y.H. Ding. "Nanoimprint Lithography". In: Feb. 2010. ISBN: 978-953-307-064-3. DOI: 10.5772/8189.

[34] Clivia Sotomayor Torres. "Alternative Lithography: Unleashing the Potentials of Nanotechnology". In: Jan. 2003. DOI: 10.1007/978-1-4419-9204-8.

[35] *Thunder NIL s.r.l.* URL: https://www.thundernil.com/it/.

[36] D. Resnick. "9 - Nanoimprint lithography". In: *Nanolithography*. Ed. by Martin Feldman. Woodhead Publishing, 2014, pp. 315–347. ISBN: 978-0-85709-500-8. DOI: https://doi.org/10.1533/9780857098757.315. URL: https://www.sciencedirect.com/science/article/pii/B9780857095008500099.

[37] "Capacitive Discharges, Inductive Discharges, Etching". In: *Principles of Plasma Discharges and Materials Processing*. John Wiley and Sons, Ltd, 2005. Chap. 11,12,15. ISBN: 9780471724254. DOI: https://doi.org/10.1002/0471724254.ch11. eprint: https://onlinelibrary.wiley.com/doi/pdf/10.1002/0471724254.ch11. URL: https://onlinelibrary.wiley.com/doi/abs/10.1002/0471724254.ch11.

[38] Fouad Karouta. "A practical approach to reactive ion etching". In: *Journal of Physics D: Applied Physics* 47.23 (May 2014), p. 233501. DOI: 10.1088/0022-3727/47/23/233501. URL: https://doi.org/10.1088/0022-3727/47/23/233501.

[39] a plasma-therm company Corial. *Inductively Coupled Plasma – Reactive Ion Etching (ICP-RIE)*. URL: https://corial.plasmatherm.com/en/technologies/icp-rie-inductively-coupled-plasma-reactive-ion-etching.

[40] Slide to doc. *Reactive Ion Etching Outline Reactive Ion Etching RIE*. URL: https://slidetodoc.com/etch-systems-i-types-of-etch-systems-plasma/.

[41] Robert Charles Devlin et al. "Spin-to-orbital angular momentum conversion in dielectric metasurfaces". In: *Opt. Express* 25.1 (Jan. 2017), pp. 377–393. DOI: 10.1364/OE.25.000377. URL: http://opg.optica.org/oe/abstract.cfm?URI=oe-25-1-377.

[42] Dhirendra Kumar, Abhijit Das, and Bosanta R. Boruah. "Note: A simple experimental arrangement to generate optical vortex beams". In: *Review of Scientific Instruments* 84.2 (2013), p. 026103. DOI: 10.1063/1.4790848. eprint: https://doi.org/10.1063/1.4790848. URL: https://doi.org/10.1063/1.4790848.

[43] C. MAURER et al. "Upgrading a microscope with a spiral phase plate". In: *Journal of Microscopy* 230.1 (2008), pp. 134–142. DOI: https://doi.org/10.1111/j.1365-2818.2008.01968.x. eprint: https://onlinelibrary.wiley.com/doi/pdf/10.1111/j.1365-2818.2008.01968.x. URL: https://onlinelibrary.wiley.com/doi/abs/10.1111/j.1365-2818.2008.01968.x.